Full Length Article

Deep-red emitting SrNaZrO$_3$:Mn^{4+} phosphor for greenhouse cultivation LEDs application

A. Nathan-Abutu [a,b], I. Ahemen [b], R.E. Kroon [c], L.J.B. Erasmus [c], A. Ramirez-DelaCruz [a], A. Reyes-Rojas [a,*]

[a] *Materials Science Department. Centro de Investigacion' en Materiales Avanzados, S.C., Miguel de Cervantes 120, Complejo Industrial Chihuahua, 31109, Chihuahua, CHIH, Mexico*
[b] *Department of Physics, Federal University of Agriculture, P.M.B. 2373, Makurdi, Benue State, Nigeria*
[c] *Department of Physics, University of the Free State, P.O Box 339, Bloemfontein, 9300, South Africa*

ABSTRACT

A sequence of deep red-emitting phosphors, Sr$_{0.9}$Na$_{0.2}$Zr$_{1-x}$O$_3$:Mn^{4+}, was synthesized using a modified sol-gel method. The Rietveld analysis indicates that the optical properties are influenced by the coordination environment of the host material. The Zr atom's 4a site symmetry is occupied by Mn^{2+} and Mn^{4+} ions in an octahedral coordination, leading to a reduction in V$_o^{°°}$. When excited at 325 nm, photoluminescence (PL) at room temperature (303.15 K) and higher temperatures exhibited strong blue emission at 423 nm and a zero-phonon deep-red emission band at 698 nm. These emissions stem from the ^{4}T$_1$→^{6}A$_1$ and ^{2}E$_g$ → ^{4}A$_{2g}$ transition in the 3d orbit of manganese ions. At higher concentrations, PL intensity was quenched due to energy transfer and exchange interactions between adjacent ions. Temperature-dependent PL measurements showed a quenching in emission intensity with increasing temperature, attributed to the dominance of nonradiative transitions. The Sr$_{0.9}$Na$_{0.2}$Zr$_{1-x}$O$_3$:$_{0.01}$Mn^{4+} nanophosphors demonstrated high stability, retaining 50 % of their emission intensity at 422 K, with a thermal relative sensitivity of 2.49 %K^{-1}. The red phosphor achieved CIE color coordinates of (0.707, 0.293), comparable to commercial NTSC-standard red-emitting phosphors, with 93 % color purity. These properties make it suitable for applications in thermal optical sensors and high-power LEDs.

1. Introduction

Ensuring global food security has become an urgent priority, aiming to provide all individuals with consistent access to sufficient, safe, and nutritious food required for a healthy and active life. The escalating challenges posed by climate change and environmental degradation, particularly the effects of greenhouse gas emissions, have severely affected the efficiency of food production and its availability. Increasing temperatures and erratic weather conditions, and severe climatic events are leading to significant crop failures and reduced yields, thereby threatening food security [1]. In response, innovative approaches like employing phosphor-enhanced LED lighting in agricultural lighting are being explored [2]. These LEDs can fine-tune light spectra to maximize plant growth, leading to improved photosynthesis and higher crop yields. Additionally, phosphor LEDs offer conserving energy and minimizing environmental impact while promoting sustainable agriculture. Integrating such innovations is crucial for building robust food systems

capable of withstanding escalating climate pressures.

Inadequate lighting impairs efficient photosynthesis in plants, particularly in regions with limited sunlight, leading to etiolation. Conversely, excessive light can produce oxygen radicals and cause photoinhibition, both of which restrict primary productivity. Plants selectively absorb sunlight at specific wavelengths, with blue light (380–520 nm) and red/deep-red light (610–720 nm) being particularly important. These wavelengths are critical for vegetative growth, photosynthesis, flowering, and budding. The far-red to infrared range (720–1000 nm) contributes to plant germination and flowering, though absorption in this band is limited. Absorption in the infrared region (>1000 nm) is entirely converted to heat, which can potentially harm plants [3,4]. In addition to chlorophylls, other photosynthetic pigments, such as carotenoids (β-carotene, zeaxanthin, lycopene, and lutein), are essential for photosynthesis. These pigments, embedded in protein chlorophyll-carotenoid complexes, assist in light absorption and energy transfer to the photosystem reaction center in the chloroplast,

---

generating electrons for the photosynthetic process [5,6].

The development of fluorescent materials for light-conversion technology is primarily centered on transforming UV and yellow-green light—wavelengths that are less essential for plant growth—into blue and red light, which are more beneficial for plant development [2]. Plants grown under artificial lighting often adapt their photosynthetic processes, with light-emitting diodes (LEDs) emerging as a promising alternative light source, opening new possibilities for controlled cultivation. LEDs offer significant advantages over metal halide lights for plant growth, primarily due to their minimal radiant heat generation [7–9]. This feature allows LEDs to be placed in close proximity to, or even within, the greenhouse canopy without damaging the crops. Positioning the lights closer to the canopy enhances light delivery to nearby leaves, reducing space requirements and enabling multi-layer production systems with closely spaced shelves. Additionally, LED designs with fixtures incorporating specialized lenses and reflectors ensure that a substantial portion of the emitted light reaches the plants, resulting in more efficient use of energy, light, and coverage area [10]. LED lighting offers improved control over the spectral composition, allowing for more precise regulation of various aspects of plant performance, such as flowering time, optimal photosynthetic efficiency, and decreased susceptibility to heat stress.

In addition to rare-earth ion-doped phosphors, manganese-doped materials also show promise for red light emission. The emission band wavelength in Mn^{2+}, Mn^{3+}, and Mn^{4+} ions primarily depend on the covalent interactions with the host crystal or the surrounding crystal field, as their valence electrons are the 3d electrons. Typically, manganese exhibits green emission when in tetrahedral coordination, where the crystal field is weak. In contrast, when in octahedral coordination, which features a strong crystal field, manganese displays orange to deep red luminescence [11,12]. The Mn^{4+} ion exhibits a strong (deep) red emission when excited with visible light and has demonstrated significant potential as a replacement for the Eu^{3+} activator ion [13]. Furthermore, studies on monoclinic Li_2TiO_3:Mn^{4+} solid solutions indicate that increasing the concentration of Mn^{4+} ions relative to Mn^{2+} and Mn^{3+} leads to an enhancement of red emission, particularly around 680 nm [14].

Mn-doped $SrNaZrO_3$ possesses a perovskite crystal structure, where $(Sr^{2+}Na^+)$ and Zr^{4+} ions occupy the A and B sites, respectively. The substitution of Zr^{4+} with Mn^{4+} ions introduce energy levels within the bandgap, which influence electronic transitions. The luminescence mechanism involves energy transfer between Mn ions and the host lattice. The energy levels created by Mn facilitate the absorption and emission of light in the deep red region (approximately 650–700 nm) through radiative transitions within the Mn ions. Various factors, such as doping concentration and annealing conditions, can also affect the emission characteristics, including emission intensity, peak wavelength, and color purity [15].

$SrNaZrO_3$ was first fabricated as a new host material before incorporating manganese ions as the dopant to ensure compatibility, optimize energy transfer, improve emission efficiency, and enhance stability, as outlined in our previous article [16–18]. It also helps tune the optical properties and minimize non-radiative losses, enhancing the overall performance of the luminescent material. The investigation focused on the influence of manganese doping concentration on both the crystal structure and luminescent properties. The study sought to assess the potential use of $SrNaZrO_3$:Mn^{4+} phosphor material in the development of LEDs for horticultural applications, an area that has not been sufficiently explored in relation to food security. This research aims to address this gap by examining how the material's properties can improve LED technology to support plant growth and development.

2. Experimental

2.1. Synthesis

A series of $Sr_{0.9}$ $Na_{0.2}Mn_xZr_{1-x}O_3$ ($0.01 \leq x \leq 0.09$) perovskite nanophosphors were prepared by the wet chemical reaction method. Typically, the synthesis involved using the following starting materials; Zirconium (IV) 2,4-pentanedionate ($ZrC_{20}H_{28}O_8$), strontium nitrate Sr $(NO_3)_2$, sodium nitrate ($NaNO_3$), Manganese(II) nitrate tetrahydrate ($Mn(NO_3)_2 \cdot 4H_2O$), citric acid ($C_6H_8O_7.H_2O$), and ethylene glycol ($C_2H_6O_2$). The citric acid with a molar concentration of 2 M was used as fuel and ethylene glycol (3 M) as gelatin agent. Our earlier report provides a detailed procedure for the synthesis of $Sr_{0.9}Na_{0.2}ZrO_3$ [16]. For the doped compounds, $Mn(NO_3)_2 \cdot 4H_2O$ at varying concentrations of 1, 3, 5, 7, and 9 % was used, subsequently identified as Mn1,Mn3, Mn5, Mn7 and Mn9, respectively.

2.2. Instrumentation

The samples' powder X-ray diffraction (XRD) patterns were obtained by using a Bruker D8 Discover diffractometer, which works on the Bragg-Brentano focusing geometry. The diffractometer utilizes a Cu-Kα radiation source with a wavelength of 5.406 Å. The instrument was set to operate at a voltage of 40 kV and a current of 30 mA. The XRD patterns were collected at a scan rate of 1° per minute. The structural properties were further obtained using a JEM-2200FS JOEL transmission electron microscope (TEM) equipped with a field emission gun (FEG) operating at an accelerating voltage of 200 kV. For high-resolution transmission electron microscopy (HRTEM), the samples were suspended in isopropanol and a drop was placed on a carbon-coated copper TEM grid and dried under a UV lamp. The surface morphologies of the prepared nanophosphor particles, along with the stoichiometric proportions of the constituent ions from elemental analysis, were examined using JEOL-JSM-7401F field emission scanning electron microscope (FESEM), equipped with energy dispersive X-ray spectroscopy (EDX). Diffuse reflectance spectra were obtained using a Thermo Scientific Evolution 220 model of UV–Vis spectrophotometer. The reflectance curves were gathered over a range of 190–1100 nm. In photoluminescence experiments, including temperature dependent measurements, a 325 nm He-Cd laser was used as the excitation source. The lifetime and quantum yield measurements were made using an Edinburgh Instruments FLS980 Fluorescence Spectrophotometer. X-ray photoelectron spectroscopy (XPS) measurement was conducted using a Thermo Scientific K-Alpha X-ray Photoelectron Spectrometer with monochromatic A1 Kα radiation (hυ = 1486.68 eV). The XPS spectra presented in this study were referenced to the C1s peak at 284.91 eV.

3. Results and discussion

3.1. Crystal structure and crystal-size analyses

Fig. 1 shows the XRD patterns of $Sr_{0.9}Na_{0.2}Zr_{1-x}O_3$:$Mn^{4+}$ ($x = 0.01 \leq x \leq 0.09$) nanophosphors. All the diffraction peaks were indexed to the orthorhombic structure of $SrZrO_3$ based on the JCPDF number 044–0161. The intense and sharp peaks implied the high crystallization of $SrNaZrO_3$:Mn^{4+} phosphors. The expectation is that Mn^{2+} ions (ionic radius, 0.67 Å) and Mn^{4+} ions (ionic radius, 0.53 Å) substituted Zr^{4+} ions (ionic radius, 0.72 Å) in the crystal lattice owing to their closely matched ionic radii in the six-coordination number (CN = 6) [19]. As illustrated in Fig. 1(b), the (121) peak centered around 30.82° experiences a shift toward higher angles as the concentration of Mn increased. The displacement of the (121) peak towards higher angles suggests a contraction in lattice constants as confirmed by the reduction of the unit cell volume (Table 1).

The Goldschmidt's tolerance factor *t*, which determines the degree of disorder or stability in an ABO_3-type perovskite was calculated for
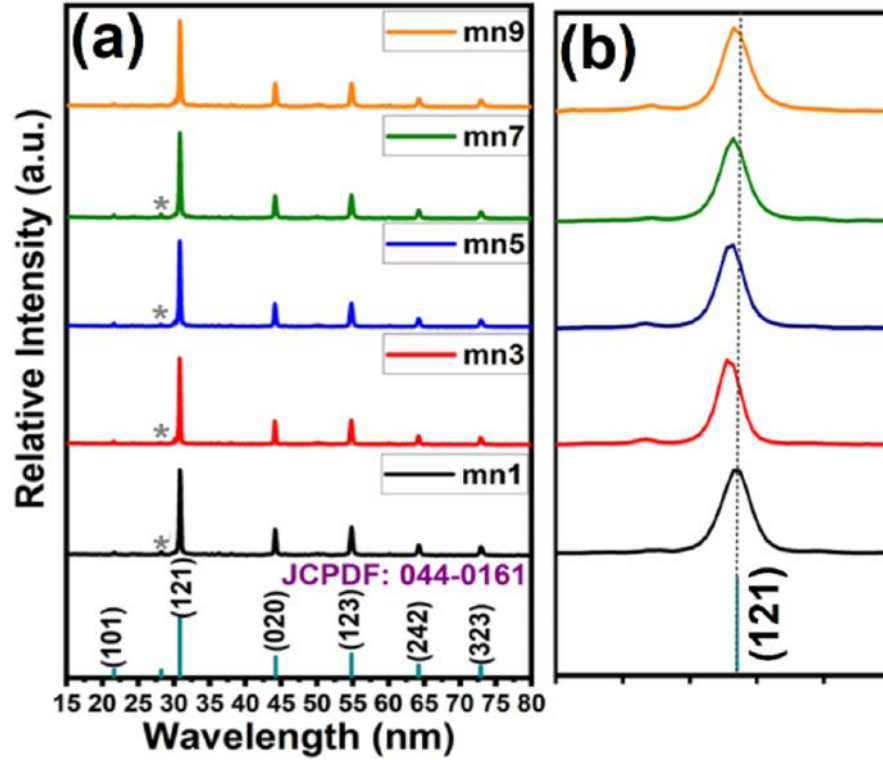
Fig. 1. (a) XRD patterns and (b) XRD peak shift at $2\theta = 30.82°$ for SrNaZrO$_3$:Mn^{4+} nanoparticles.

Table 1
Rietveld refined crystal structure parameters of SrNaZrO$_3$:Mn^{4+} nanophosphors.

Parameter	S.G	Composition				
		0.01	0.03	0.05	0.07	0.09
a	*Pnma*	5.80763	5.80573	5.80252	5.80449	5.80566
b		8.19681	8.19357	8.19693	8.19213	8.19073
c		5.79187	5.79167	5.79038	5.78963	5.78863
Vol. (Å^3)		275.716	275.508	275.407	275.304	275.265
Con. (%)		94.16	95.5	94.98	95.54	95.26
a	*P4$_2$/nmc*	3.60009	3.5949	3.60053	3.60111	3.59781
b		5.21955	5.20665	5.20955	5.19725	5.19279
Vol. (Å^3)		67.649	67.287	67.536	67.398	67.217
Con. (%)		4.65	1.31	3.49	1.33	3.88
a	*P2$_1$/c*	5.15057	5.14554	5.14869	5.15356	5.15776
b		5.20578	5.20041	5.2058	5.20986	5.20641
c		5.33349	5.32312	5.33983	5.32403	5.31943
β		99.28658	99.14503	99.17652	99.19634	98.45911
Vol. (Å^3)		141.131	140.63	141.292	141.109	141.291
Con. (%)		1.19	3.19	1.53	3.13	0.86
χ^2		1.79	1.55	1.72	1.78	1.79
Mn-O (A)		2.0886	2.0885	2.0875	2.0857	2.0848
t		0.9241	0.9246	0.9250	0.9254	0.9259

Sr$_{0.9}$Na$_{0.2}$Zr$_{1-x}$O$_3$: xMn^{4+} (x = 0.01, 0.03, 0.05, 0.07, and 0.09) using the following expression [17,20]:

$$t = \frac{(0.9R_{Sr} + 0.2R_{Na} + R_O)}{\sqrt{2}((1 - x)R_{Zr} + xR_{Mn} + R_O)} \tag{1}$$

where, R_{Sr}, R_{Na}, R_{Zr}, R_{Mn} and R_O represent the ionic radii of Sr^{2+}, Na$^+$, Zr^{4+}, Mn^{2+}, Mn^{4+} and O^{2-} ions, respectively. The calculated tolerance factor for all samples displays a monotonic increment from 0.9241 to 0.9259 with increasing Mn concentrations (Table 1), confirming the relative stability of the orthorhombic structure of the perovskite.

Further structural elucidation was achieved through Rietveld refinement of the XRD sample data using the Full Prof suite software.

The refined results indicate the presence of three structures: approximately 95 % orthorhombic SrZrO$_3$, with the remaining approximately 5 % consisting of a mixture of tetragonal and monoclinic zirconia (Table 1). However, in order to know where the Mn atom was positioned into the orthorhombic structure, two Rietveld refinement strategies were used, one where the *4c* site symmetry multiplicity of the Sr is partially occupied by the Mn atom and another where the *4a* site symmetry multiplicity of the Zr atom is occupied by Mn. The Rietveld refinement analysis indicated a goodness of fit (χ^2) above 2 for the Mn atom partially replacing site *4c*, while in site *4a*, it reached a goodness of fit below 2; therefore, the precision of the statistical model concludes that the Mn partially replaces only the Zr atom in the orthorhombic *Pnma* symmetry. Fig. 2(b) displays a representative graphical output of
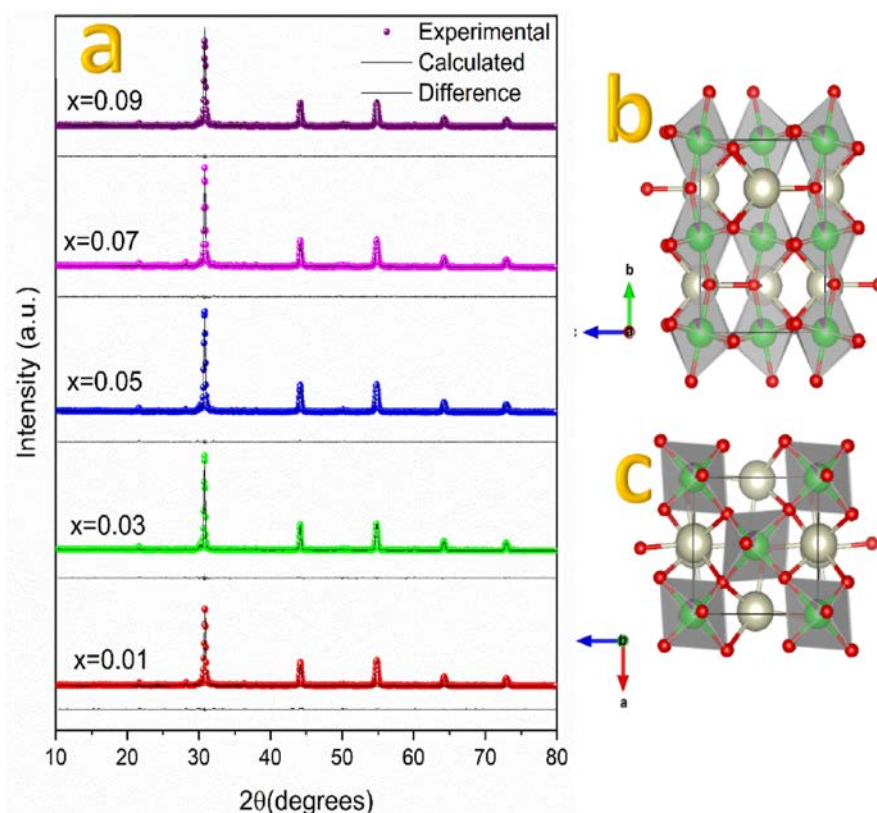
Fig. 2. (a) Rietveld refined XRD pattern of SrNaZrO$_3$:Mn^{4+} nanophosphor, (b) and (c) schematic structure model of Sr$_{0.9}$Na$_{0.2}$Zr$_{0.91}$Mn$_{0.09}$O$_3$ crystal octahedral tilt.

the Rietveld refined XRD data. The good matching between the observed and refined data confirms the orthorhombic phase of all Mn-doped SrNaZrO$_3$ phosphors. Table 1 presents the refined lattice parameters (*a, b, c*), cell volume (Å^3), phase concentration, and goodness of fit (χ^2). As shown in Table 1, the lattice parameters and unit cell volume decrease with the substitution of Mn in the SrNaZrO$_3$ lattice. As expected, the bonding length between manganese and oxygen decreases as Mn increases in the solid solution, consistent with the cell volume trend. It results in lattice strain in the Mn-doped SrNaZrO$_3$ solid solution due to the mismatch in the ionic radii of Mn and Zr ions [21]. To create a 3D polyhedral structure model using VESTA software, the CIF file obtained for the orthorhombic phase from the final refinement of the phosphor was used. The typical schematic model showing octahedra orientation for the composition with x = 0.09 is displayed in Fig. 2(b) and (c). From Rietveld results, for the orthorhombic structure view along [100] and [010] crystallographic directions shown in Fig. 2(b) and c, the octahedra frame turns along [010] and tilts from the [*hkl*] direction. Considering the [111] direction for a pseudo-cubic structure, the MnO$_6$ octahedra tilt by 13.88, 13.77, 13.70, 13.54, and 13.39° for Mn1, Mn3, Mn5, Mn7 and Mn9, respectively. This continuous decrease in the octahedral tilt angle indicates increased lattice distortion. These results are inconsistent with the increase in Goldschmidt's tolerance factor (geometrical); therefore, the lattice distortion may be influenced strongly by point defects. Additionally, the presence of impurity phases of tetragonal and monoclinic zirconia may account for the discrepancies observed between the two results. To investigate this further, XPS analysis was conducted on the samples to identify point defects. The most prominent diffraction peaks were utilized to calculate the average crystallite size using Scherrer's equation [22,23]. The resulting average crystallite sizes were 31, 25, 27, 26, and 24 nm for Mn1, Mn3, Mn5, Mn7, and Mn9 samples, respectively.

3.2. X-ray photoelectron spectroscopy (XPS)

Fig. 3(a) shows that the entire standard XPS survey spectrum (100–1100 eV) of the synthesized material revealing the existence of strontium (Sr), zirconium (Zr), sodium (Na), manganese (Mn), and oxygen (O) elements. Fig. 3 (b, c, d, e, f) display the high-resolution XPS spectra of Sr 3d, Zr 3d, O 1s, Mn 2p, and Na 1s, along with their respective Gaussian curve fits. These spectra were generated using the CASA-XPS software, employing a standard U2 Tougarrd baseline for all measurements. The detection of the C 1s peak at 284.91 eV in the XPS spectrum functions as the internal reference point for calibrating binding energy, attributed to adventitious carbon originating from the XPS instrument.

Fig. 3(b) displays the detailed high-resolution scan of the Sr 3d peaks [24], with the Sr 3d$_{5/2}$ and Sr 3d$_{3/2}$ peaks observed at 132.61 and 134.37 eV, respectively, bonded with zirconate ions. The binding energies corresponding to Zr 3d$_{3/2}$ and Zr 3d$_{5/2}$ are 183.26 and 180.97 eV, respectively, as shown in Fig. 3(c). The spectra of Sr and Zr in their 3p and 3d orbitals confirm the Sr^{2+} oxidation state and Zr in the Zr^{4+} oxidation state [25]. Fig. 3(d) depicts the observed difference in binding energy for oxygen in the O^{2-} oxidation state, corresponding to 1s spectra. Specifically, the spin-orbit split peaks at 531.26 eV represent absorbed oxygen in the SrNaZrO$_3$, while those at 529.11 eV correspond to lattice oxygen associated with O^{2-} ions [26].

The peaks observed in the Mn 2p spectrum (Fig. 3(e) at 653.64 and 642.18 eV are assigned to Mn(2+) 2p$_{1/2}$ and Mn(2+) 2p$_{3/2}$, respectively. As can be seen in Fig. 3(e), the Mn1 sample presents a shift of these signals to low binding energy with broader peaks, which is due to the presence of Mn^{2+} and Mn^{4+} oxidations states (Mn^{4+}at 641.9 eV) [27]. It is evident that Mn^{2+} oxidation states can induce oxygen vacancies, while Mn^{4+} compensates for V$_o^{\circ\circ}$ by replacing Zr^{4+} ions. From a charge-compensation perspective, the orthorhombic perovskite requires
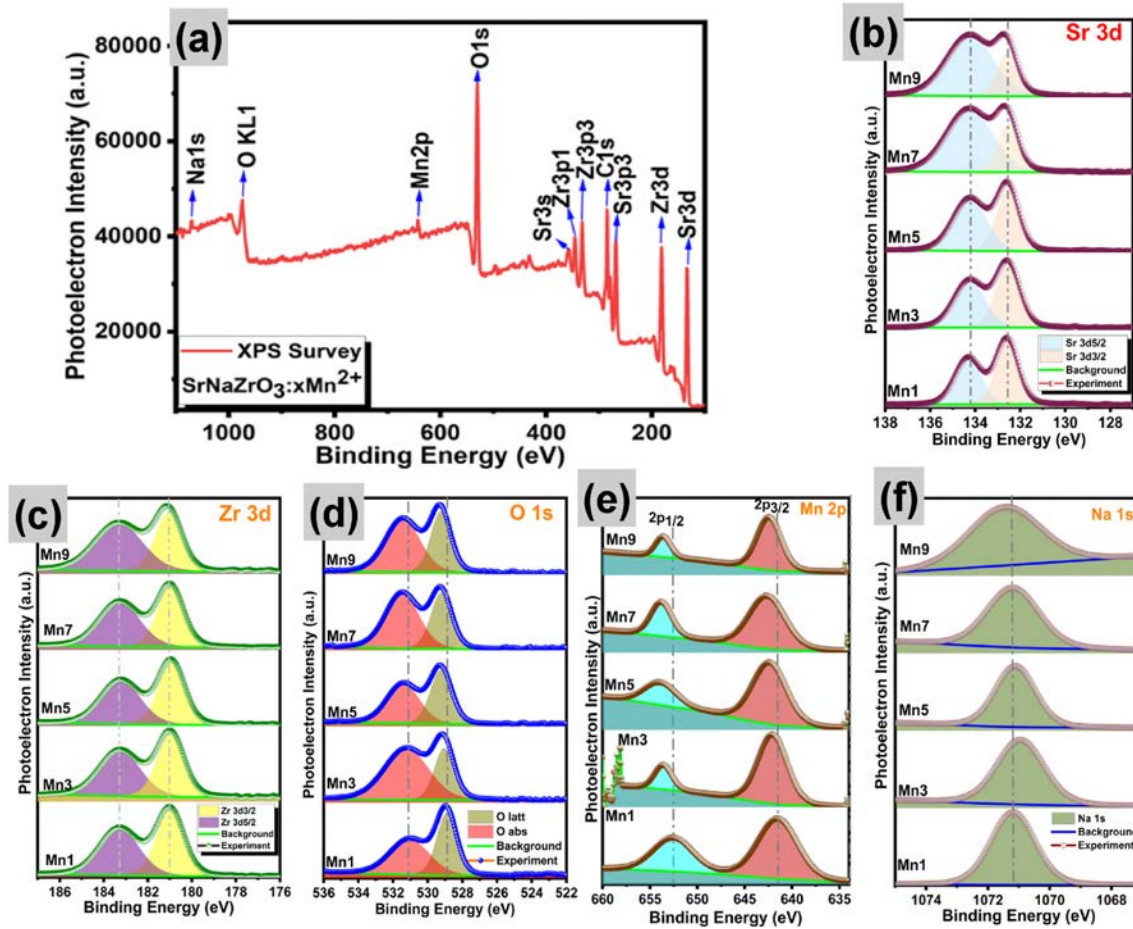
Fig. 3. XPS spectra of (a) SrNaZrO$_3$:Mn^{4+} survey, (b) Sr 3d, (c) Zr 3d, (d) O 1s, (e) Mn 2p, (f) Na 1s peaks.

Mn^{4+} oxidation states to stabilize the Zr^{4+} sites, as Mn^{2+} tends to induce more $V_o^{\circ\circ}$. As shown in Fig. 3(e), the broadening of the Mn 2p$_{3/2}$ peak decreases with increasing manganese concentration in the solid solution, leading to a reduction in Mn^{4+} oxidation states at 641.9 eV. Consequently, the concentration of Mn^{2+} ions increase, which in turn enhances disorder through the formation of oxygen vacancies, consistent with the Rietveld analysis results. Modifying the calcination conditions allows for control over the valence states of manganese ions, which in turn affects the optical properties of the material. Calcining SrNaZrO$_3$: Mn^{4+} solid solution in different atmospheres resulted in changes to the valence states of manganese ions in the luminescent powders. The calcination environment, whether oxidative or reductive, influences manganese's oxidation state. For example, a reducing atmosphere can lower the oxidation state, increasing the Mn^{2+} concentration, while an oxidizing atmosphere (such as air, as used in this research) can raise the oxidation state, favoring Mn3+ or Mn4+ [28–30]. The Mn^{2+} ion generated by the chemical reaction in the octahedral site of the perovskite structure can also be oxidized electrochemically to Mn^{4+} in an oxygen atmosphere at high temperature according to the equation: Mn^{2+} + O$_2$ → MnO$_2$ + 4e. However, it is limited by the maximum oxygen coordination in the octahedral site properly in the local structure BO$_6$ [31–33].

As shown in Fig. 3(f), the measured binding energy at 1070.74 eV corresponds to Na 1s. Another notable observation is the blue shift of the Na 1s peak, which moves from 1070.74 eV to 1071.17 eV, as illustrated in Fig. 3(f). This blue shift is more pronounced in the Na 1s peak than in the O 1s peak, likely due to the significant electronegativity difference (3.44 - 0.93 = 2.51) between oxygen and Na$^+$ ions, as well as the

relaxation occurring within the Na-O bonding environment [34,35].

In order to assess the trend of oxygen vacancy, the O$_{abs}$/O$_{latt}$ ion ratios [36] were calculated from the O 1s peaks fitting, resulting in 0.7290, 0.9893, 0.9708, 0.9904, and 0.9204 for Mn1, Mn3, Mn5, Mn7, and Mn9 samples respectively. Sample Mn1 exhibits the lowest concentration of oxygen vacancies consistent with XRD Rietveld analysis for low lattice distortion, as the Mn concentration increases in the solid solution increases the disorder by the oxygen vacancies, due to the concentration reduction of the Mn^{4+} ions and to the rise of Mn^{2+} concentration.

3.3. Optical bandgap properties

Fig. 4(A) displays the diffuse reflectance spectra of SrNaZrO$_3$ samples doped with different concentrations of manganese. The Mn1 sample showed two absorption bands at 323 nm and 365 nm. The optical energy band gap of the nanophosphors was determined using a combination of the Kubelka-Munk and Tauc's-Wood relations [37–39]:

$$F(R) = \frac{A(h\nu - E_g)^n}{h\nu} \tag{2}$$

$$F(R) = \frac{(1-R)^2}{2R} = \frac{K}{S} \tag{3}$$

where $h\nu$ is the photon energy, A is a constant related to the properties of the valence and conduction bands, the exponent 'n' is ½, 2, 3/2 and 3 for allowed direct, allowed indirect, forbidden direct and forbidden indirect transitions respectively [37,39], and E_g is the energy band gap. Also, R,
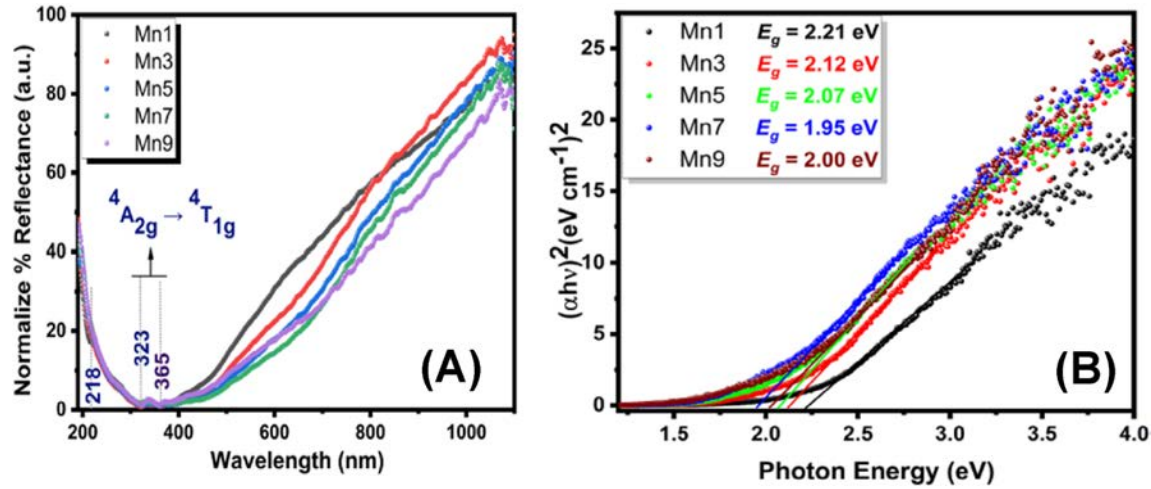
Fig. 4. (A) Normalized Diffuse Reflectance, (B) Band gap energies spectra of $SrNaZrO_3:Mn^{4+}$ nanophosphors.

K, and S are the reflectance, absorption, and scattering coefficient, respectively.

The optical band gap energy values were obtained from the points on the $h\nu$ axis, where the extrapolated linear fit of the $[F(R)h\nu]^2$ verses $h\nu$ plots gave $[F(R)h\nu]^2 = 0$ (Fig. 4(B)). The obtained energy bands values for Mn-doped $SrNaZrO_3$ samples Mn1, Mn3, Mn5, Mn7, and Mn9 are 2.21 eV (561 nm), 2.12 eV (585 nm), 2.07 eV (599 nm), 1.95 eV (636 nm) and 2.0 eV (620 nm), respectively. The optical band edge and the optical band gap are both controlled by structural order-disorder in $SrZrO_3$-like perovskite lattice. An ordered perovskite structure has all its electrons bonded such as ZrO_6 in the octahedral site. However, a distorted/disordered structure such as ZrO_5 with unbound electrons generate oxygen vacancies ($V_o^{\circ\circ}$) which form localized sates in the host band gap. The substitutional doping of Mn^{2+} at Zr^{4+} effectively create $[ZrO_5, V_o^{\circ\circ}]$ clusters because of the differences in their valence number and ionic radii. Thus, the narrowing of the optical band gap suggests a decrease in the structural order and formation of localized energy states in host band gap. The induced oxygen vacancies trap electrons, creating donor states near the valence band (VB). As the concentration of oxygen vacancies increases due to increase in Mn, there is a positive adjustment of the VB edge, leading to the narrowing of the optical band gap [40,41]. Also, a comparative analysis of these phosphors reveals a direct correlation between luminescence intensities and factors such as crystallite size, optical band gap, cell volume, and oxygen vacancies, as illustrated in Fig. 4 (C1 and C2).

3.4. Field emission scanning and high-resolution transmission electron microscopy studies

The field emission scanning electron micrographs (FE-SEM) of $SrNaZrO_3:Mn^{4+}$ at various manganese concentrations, along with the compositional analysis using EDX, are presented in Fig. 5(a–e). The images reveal clusters of nearly spherical particles within the nanometer size range of 48 nm–58 nm that are interconnected. This connected microstructure results from partial sintering of the materials. Notably, as the manganese concentration increases, the powders appear slightly coarser and larger, indicating that manganese may facilitate the sintering process. The elemental analysis data for the $SrNaZrO_3:Mn^{4+}$ nanophosphors are summarized in the table inset of Fig. 5(f), which shows the atomic percent of all elements (Sr, Zr, Na, O, and Mn) constituting the compound.

TEM analysis was additionally conducted to further explore the microstructure of representative sample, specifically $Sr_{0.9}Na_{0.2}Zr_{0.99}O_3:_{0.01}Mn^{4+}$ (or Mn1) sample. As depicted in Fig. 6(a) and (b), the particle size was approximately 35 nm, and they exhibited a tendency to aggregate. A representative high-resolution TEM image [Fig. 6(c)] once again illustrates the crystalline nature of the sample. The lattice fringe spacing values in Fig. 6(d) [[0.409, 0.357, 0.283, 0.179 nm]] correspond to Miller indices (hkl) of 101, 111, 121, and 113, respectively, aligning well with those determined from the SAED patterns Fig. 6(e).
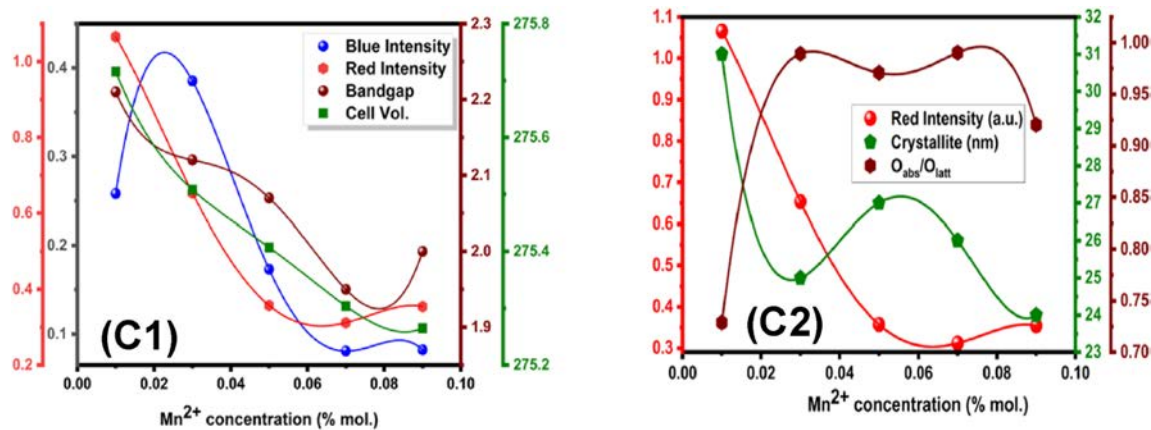

Fig. 4. (C1, C2). Relative emission intensity of blue emission, red emission band, cell volume, optical bandgap, crystallite size and Oabs/Olatt for different Mn^{4+} concentration in $SrNaZrO_3$ phosphors.
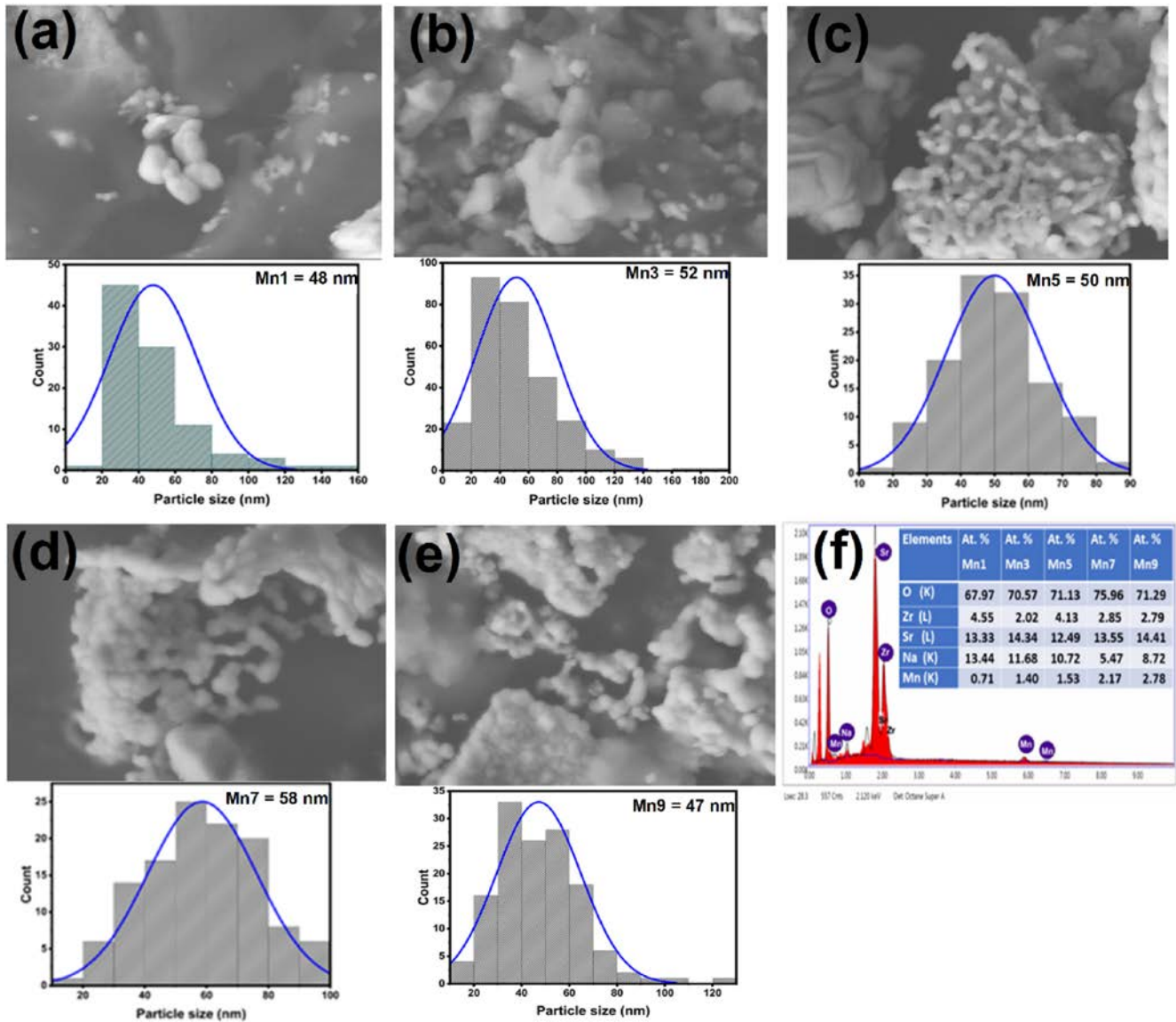
Fig. 5. FE-SEM images and average particles sizes histogram of (a–e) for Mn1 to Mn9 powders; (f) EDS spectrum of Mn1 sample and EDS At. % of Mn1 to Mn9 (insert table).

3.5. Photoluminescence studies

3.5.1. Excitation spectrum

The photoluminescence excitation spectrum obtained at room temperature (emission at 689 nm) for SrNaZrO$_3$ nanocrystals doped with 0.01 M ratio of Mn^{4+} is displayed in Fig. 7(b). The excitation spectrum is broad and spans the range of 260–600 nm. Three broad peaks can be conspicuously observed at about 333, 374, and 560 nm. However, upon deconvolution of the excitation spectrum using Gaussian function, we observed peaks at 333 (30,035 cm^{-1}; T$_1$), 374 (26,742 cm^{-1}; T$_2$), 414 (24,158^{-1}; T$_3$), and 560 nm (14,329 cm^{-1}; T$_4$). The T1 peak is assigned to the Mn^{4+} - O^{2-} charge transfer band (CTB) [42]. This band is known to dominate the excitation/absorption spectrum. In order to assign the peaks to some transitions of Mn^{4+} in our host matrix, the Tanabe Sugano (T-S) diagram (Fig. 7(b)) for the d^3 electronic configuration in an octahedral crystal field was utilized. According to the spin selection rule, transition involving change of multiplicity during an optical excitation process is spin-forbidden whereas, the transition with the same multiplicity is spin-allowed and dominates in intensity. Following from this

rule and from the T-S diagram, the excited states with the same multiplicity as the ground state (^{4}A$_{2g}$) are ^{4}T$_{2g}$(F), ^{4}T$_{1g}$(F), and ^{4}T$_{1g}$(P). Therefore, we expect the following transitions from our excitation spectrum; ^{4}A$_{2g}$ → ^{4}T$_{2g}$(F), ^{4}A$_{2g}$ → ^{4}T$_{1g}$(F), and ^{4}A$_{2g}$ → ^{4}T$_{1g}$(P). The ratio of the high energy band, ($\nu_2 = 26{,}742$ cm^{-1}) to lower energy band, ($\nu_1 = 17{,}860$ cm^{-1}) gives 1.50 which corresponds to the difference between the ^{4}T$_{2g}$(F) and ^{4}T$_{1g}$(F) transitions (vertical line drawn on Fig. 7(b)). Thus, we assign the T2 peak and T4 peak to the ^{4}A$_{2g}$ → ^{4}T$_{2g}$(F) and ^{4}A$_{2g}$ → ^{4}T$_{2g}$(F) spin-allowed transitions in the excitation spectrum, respectively. Meanwhile, the T3 is assigned to the ^{4}A$_{2g}$ → ^{2}T$_{2g}$ spin-forbidden transition. It is worth noting that the assignment of the 374 nm (26,742 cm^{-1}) band to the ^{4}A$_{2g}$ → ^{4}T$_{2g}$(F) transition is often contested because of the overlap with the CTB [43].

The photoluminescence emission spectra (PL) of the synthesized SrNaZrO$_3$:Mn^{4+} nanophosphors upon excitation by a 325 nm laser source are displayed in Fig. 8(a). The PL spectra exhibit two broad bands; 350–550 nm (blue) with peak maximum at about 423 nm and 650–900 nm (red) with peak maximum at 698 nm. The deep red emission band at 698 nm is dominant and corresponds to the spin-forbidden
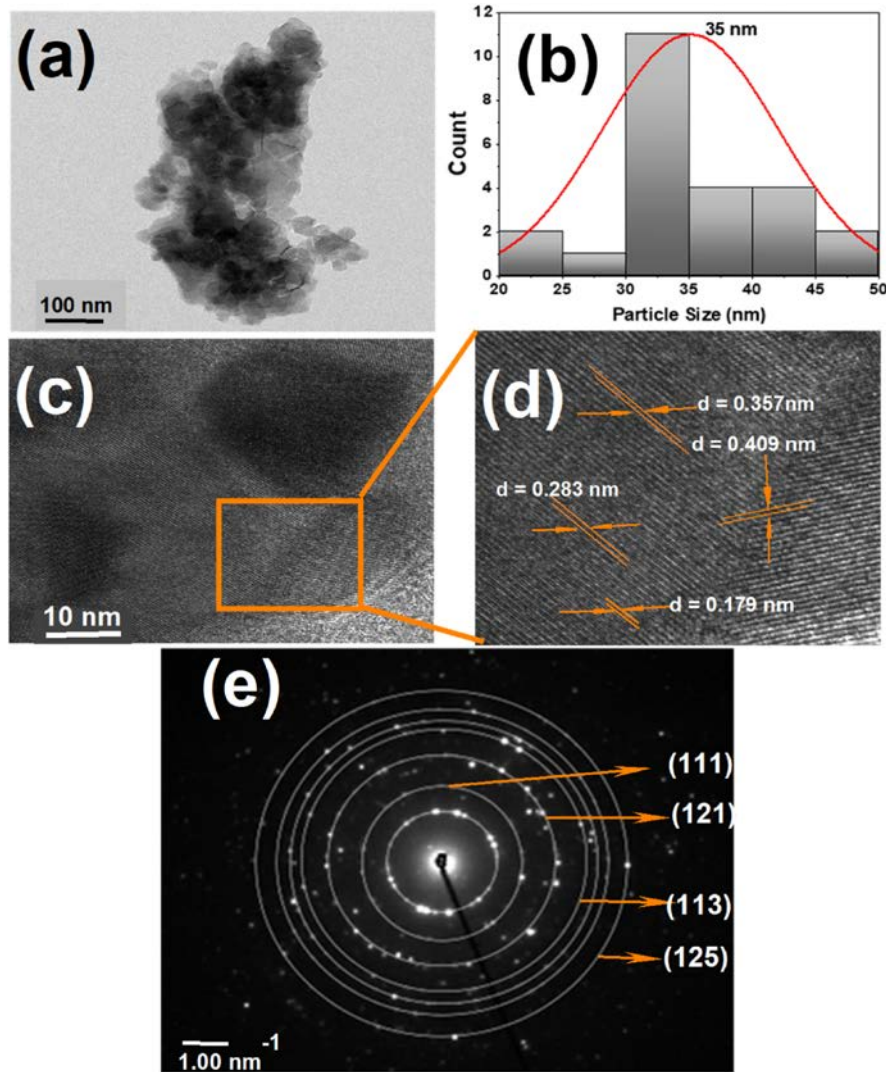
Fig. 6. (a) TEM image of Mn3 powders, (b) particle size distribution (c,d) image showing individual particles (Lattice image), and (e) corresponding selected area electron diffraction (SAED).

$^2E_g \rightarrow {}^4A_{2g}$ transition of Mn^{4+} ion. The $^4T_{1g} - {}^6A_1$ transition of the Mn ion, though parity spins forbidden is made partially electric dipole allowed by perturbations in the host crystal field induced by the distorted lattice [44,45]. The red emission band at 698 nm corresponds closely to the deep-red light absorption of phytochrome, making the synthesized $SrNaZrO_3$:Mn^{4+} nanophosphors particularly well-suited for indoor plant cultivation applications.

Also observed in Fig. 8(a) is that the peak intensity of the $^2E_g \rightarrow {}^4A_{2g}$ transition at 698 nm wavelength reduces monotonically as the Mn concentration increases. Meanwhile, the intensity of the blue emission band at 423 nm initially increases with increasing Mn concentration up to a molar ratio of 0.03 (x = 0.03) and then decreased monotonically subsequently. The observed decline in luminescence intensities of both the blue and red emission bands with increasing Mn concentration is attributed to lattice disorder and nonradiative energy transfer among the manganese ions (luminescence quenching), respectively. The spectra of $SrNaZrO_3$:Mn^{4+} samples can be effectively deconvoluted into two distinct Gaussian components, with peaks at approximately 698 nm and 801 nm (Fig. 8(b)).

To elucidate the mechanism of concentration quenching, the calculation employed the critical distance (R_c) based on the Dexter-Schulman theory, utilizing the following equation [46]:

$$R_c = 2[3V/(4\pi x_C Z)]^{\frac{1}{3}} \qquad (4)$$

where x_C is the critical content of Mn ($x_C = 0.01$), Z is the number of available sites in a unit cell ($N = 4$), and V is the volume of a unit cell (V = 275.716 $Å^3$). Thus, the critical distance (R_c) of Mn in $SrNaZrO_3$ is calculated to be 23.04 Å, which is greater than 5 Å. Therefore, the mechanism of energy transfer among manganese ions is affirmed to be a multipolar interaction. The energy transfer mechanism was calculated and the log (I/x) vs log (x) values were included the supplementary material (S2).

3.5.2. Crystal field analysis

There are basically two routes to obtaining the crystal field strength (10Dq) and Racah parameters B and C of a system i.e., the graphical method and the algebraic method. In the graphical method we shall consider two pairs of transitions $^4A_{2g} \rightarrow {}^4T_{1g}(F)/{}^4A_{2g} \rightarrow {}^4T_{2g}$ (F) and $^2E_g \rightarrow {}^4A_{2g}(F)/{}^4A_{2g} \rightarrow {}^4T_{2g}(F)$ i.e., the first pair involving both spin-allowed transitions in excitation spectrum and the second pair having one spin-allowed transition in the excitation spectrum ($^4A_{2g} \rightarrow {}^4T_{2g}$) and the other spin-forbidden transition ($^2E_g \rightarrow {}^4A_{2g}$) from the emission spectrum. The use of $^2E_g \rightarrow {}^4A_{2g}(F)$ and $^4A_{2g} \rightarrow {}^4T_{2g}(F)$ transition pair was reported by
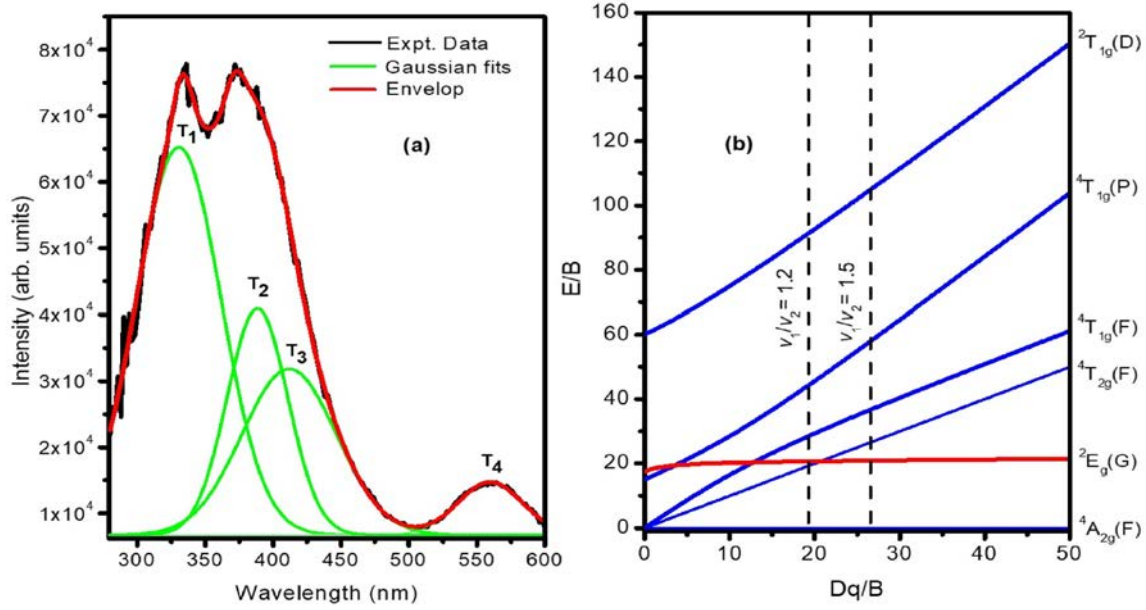
Fig. 7. Representative excitation spectrum (deconvoluted) for Mn1 sample and (b) Tanabe Sugano diagram for d^3 configuration system.
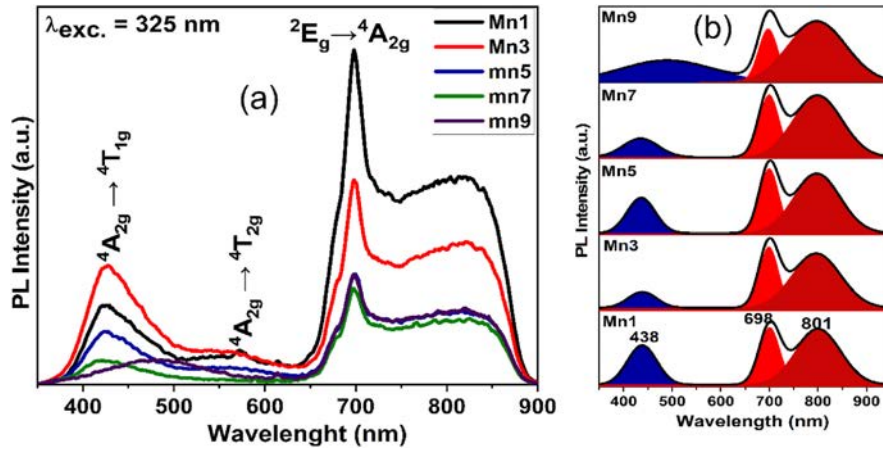

Fig. 8. (a) Emission spectra, and (b) Deconvolution of PL emission spectrum of SrNaZrO$_3$:Mn^{4+} phosphor.

Cho and Lee [47] for Mn^{4+}-doped SrZrO$_3$. First, considering the energies of the two spin-allowed transitions in the PLE spectrum; $^4A_{2g} \rightarrow {}^4T_{1g}$ (v_2 = 26,742 cm^{-1}) and $^4A_{2g} \rightarrow {}^4T_{2g}$ (v_1 = 17,860 cm^{-1}), we estimated the crystal field strength, 10Dq from the relation, $10Dq = E(^4A_{2g} \rightarrow {}^4T_{2g})$ to be 17,860 cm^{-1} or crystal field splitting, $Dq = 1786$ cm^{-1}. The ratio v_2/v_1 is approximately 1.5, which from the T-S diagram gives $v_2/B = 28.7097$ and $v_1/B = 19.2337$ corresponding to $Dq/B = 19.3515$. With these values, the average value of B was calculated to be 930 cm^{-1}. Following the same procedure outline above, but now with the pair; $^2E_g \rightarrow {}^4A_{2g}$ (v_2 = 14,329 cm^{-1}) and $^4A_{2g} \rightarrow {}^4T_{2g}$ (v_1 = 17,860 cm^{-1}), the ratio $v_1/v_2 = 1.2$ giving $Dq/B = 26.6498$. These transitions gave average B value of 677 cm^{-1}. For the algebraic method we again consider the $^4A_{2g} \rightarrow {}^4T_{1g}$(F) and $^4A_{2g} \rightarrow {}^4T_{2g}$(F) with energies $v_2 = 26,742$ cm^{-1} and $v_1 = 17,860$ cm^{-1}, respectively. Applying the following algebraic equations presented by Duo [48] for a d^3 configuration;

$$B = \frac{(v_2 - 2v_1)(v_2 - v_1)}{3(5v_2 - 9v_1)} \quad (5)$$

where,

$$v_1 = E(^4A_2 \rightarrow {}^4T_2) = 10Dq \quad (6)$$

$$v_2 = E(^4A_2 \rightarrow {}^4T_1) = \left(\frac{15}{2}\right)B + 15Dq$$
$$- 1 \bigg/ 2\left(225B^2 + 100Dq^2 - 180qB\right)^{1/2} \quad (7)$$

the values of Dq and B were evaluated as 1786 cm^{-1} and 983 cm^{-1}, respectively. We also calculated the value of B to be 983 cm^{-1} using the expressions reported by Kai Li et al. [49]. Thus, from four approaches we have the following B values; 930 cm^{-1} (graphical solution), 983 cm^{-1} (algebraic solution), 983 cm^{-1} (algebraic solution) using the $^4A_{2g} \rightarrow {}^4T_{1g}$(F)/$^4A_{2g} \rightarrow {}^4T_{2g}$ (F) transitions pair, and 677 cm^{-1} (graphical solution) arising from the $^2E_g \rightarrow {}^4A_{2g}$(F)/$^4A_{2g} \rightarrow {}^4T_{2g}$(F) transition pair. Moreover, the method involving algebraic solutions is said to produce more accurate result [48], therefore, we consider the B value of 983 cm^{-1} to be the correct value for Mn^{4+}-doped SrNaZrO$_3$ nanocrystals. Thus, using the B value of 983 cm^{-1} and Dq value of 1786 cm^{-1}, we evaluated the C value as 2471 cm^{-1}. Table 2 shows the comparison of Dq, Racah parameters B and C with other perovskite host structures

Table 2

Racah parameters (B, C), nephelauxetic ratio (β), crystal field splitting (Dq), energy of the $^2E_g \rightarrow {}^4A_{2g}$ emission transition (E: ^2Eg) in SrNaZrO$_3$ perovskites.

Perovskite	B (cm^{-1})	C (cm^{-1})	$\beta = B/B_0$	C/C_0	Dq (cm^{-1})	E: ^2E_g (cm^{-1})	Reference
SrTiO$_3$	735	2812	0.63	0.65	1820	13792	[51]
BaTiO$_3$	738	2820	0.64	0.66	1780	13861	[52]
CaZrO$_3$	754	3173	0.65	0.74	1850	15074	[53,54]

containing Mn^{4+} ion. The high value of B for SrNaZrO$_3$ indicates a relatively high ionic character of the Mn^{4+} - O^{2-} bonding in SrNaZrO$_3$ perovskite [50]. The nephelauxetic effect represented by β shows higher value for SrNaZrO$_3$ compared to the other perovskites presented in Table 2. This is a confirmation that the SrNaZrO$_3$ is more ionic than SrZrO$_3$ and the other listed perovskites due to the presence of Na $^+$ ion. The 10Dq value is larger when the covalency (or hybridization) between the metal – oxygen orbitals are stronger [47], suggesting that the smaller value (10Dq = 17860 cm^{-1}) obtained for SrNaZrO$_3$ is a result of its higher ionicity.

3.6. Photoluminescence decay lifetime analysis

Fig. 9 presents room temperature PL decay curves of SrNaZrO$_3$:Mn^{4+} samples with varying Mn^{4+} concentrations for the $^2E_g \rightarrow {}^4A_{2g}$ transition (698 nm) under 325 nm excitation. The decay curves were fitted with a second order exponential function given by;

$$I(t) = A_1 \exp\left(-t/\tau_1\right) + A_2 \exp\left(-t/\tau_2\right) \tag{8}$$

where I(t), A_1 and A_1, and τ_2 and τ_2 represent the fluorescence intensity at time t, constants, and fast and slow decay, respectively. The average values, τ_{ave} of the fast and slow decays were calculated using the following equation [55,56]:

$$\tau_{ave} = \frac{\int_0^\infty I(t)t\,dt}{\int_0^\infty I(t)\,dt} \tag{9}$$

The calculated average decay lifetime values as a function of Mn^{4+} concentrations are 16.42, 13.80, 13.74, 13.71, and 12.93 μs for Mn1, Mn3, Mn5, Mn7, and Mn9, respectively. The very fast decay lifetimes observed for Mn^{4+} in SrNaZrO$_3$ is a characteristic of Mn^{4+} ion and have been reported previously for different host matrixes [49,50]. The decreasing trend of decay lifetime from 16.42 μs to 12.93 μs with increasing manganese ion concentration is mainly attributed to an increase in non-radiative recombination processes, which are frequently
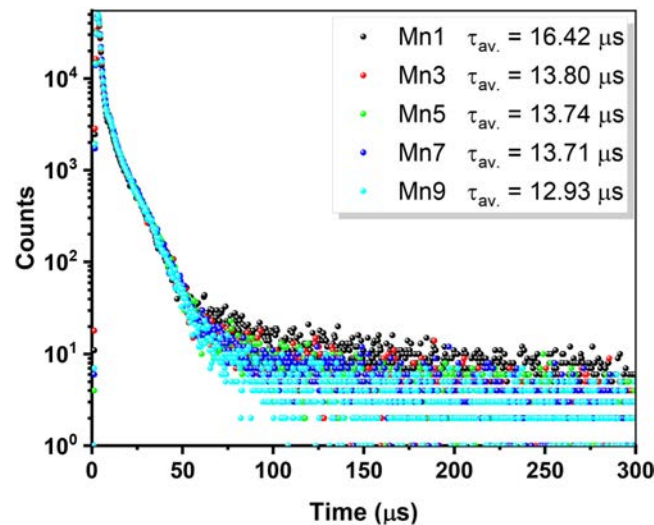
triggered by higher dopant levels, defects, or quenching centers. These mechanisms promote energy transfer through non-radiative channels, thereby shortening the duration of radiative emissions. In particular, the decline in decay lifetime is attributed to energy transfer between Mn^{4+} ions which increases at higher doping concentrations due to shortening of distance between the ions.

3.6.1. Potential application of SrNaZrO$_3$:Mn^{4+} nanophosphors to greenhouse plant growth

Few studies have demonstrated that physiological aspects of plant development, including growth, flowering time, and secondary metabolite responses, vary across species in response to specific light qualities. For instance, brief summaries of research on various plant species exposed to LEDs at specific wavelengths (640 nm–700 nm) are provided below, supporting the conclusion that SrNaZrO$_3$:Mn^{4+}, which emits deep-red light at 698 nm, serves as an efficient red phosphor source for greenhouse plant growth applications.

Tomatoes (Solanum lycopersicum): Exposure to red LEDs (660 nm) enhanced tomato yields [57]. Tomato seedlings: Using red LEDs at 660 nm and blue LEDs at 450 nm in different ratios showed that a higher Blue/Red ratio (1:0) reduced stem length [58]. Bell pepper (Capsicum annuum): Combining red LEDs at 660 nm with far-red LEDs at 735 nm (while maintaining a Photosynthetic Photon Flux of 300 μmol m^{-2}s^{-1}) promoted taller plants and increased stem biomass [59]. Chinese cabbage (Brassica rapa) treated with blue LEDs at 460 nm (11 % of total radiation) and red LEDs at 660 nm (total PPF of 80 μmol m^{-2}s^{-1}) had higher vitamin C and chlorophyll content [60]. Cabbage (*Brassica oleracea*) exposed to red LEDs (660 nm) showed increased anthocyanin levels [61]. Brassica juncea (Chinese mustard, Indian mustard, leaf mustard) exposed to red LEDs (660 and 635 nm) with blue LEDs (460 nm) delayed flowering compared to a 460 nm + 635 nm combination [62]. Kale (*Brassica oleracea*) grown under red LEDs (640 nm) pretreated with cool-white fluorescent light exhibited enhanced lutein and chlorophyll *a* and *b* levels [63]. White mustard (Sinapis alba) and green onions (spring onions or scallions) grown under red LEDs (638 nm) with an HPS lamp (90 μmol m^{-2}s^{-1}) maintaining a total PPF of 300 μmol m^{-2}s^{-1} saw increased vitamin C levels [64]. Lettuce (Lactuca sativa) and green onions grown under red LEDs (638 nm) with natural light showed reduced nitrate levels in both crops [65]. Baby lettuce (Lactuca sativa) cultivated under red LEDs (658 nm) exhibited a 6 % increase in phenolic content [66]. Green and red leaf lettuce (Lactuca sativa) grown under red LEDs (638 nm, 170 μmol m^{-2}s^{-1}) with an HPS lamp (130 μmol m^{-2}s^{-1}) had higher levels of overall phenolics and α-tocopherol [67]. Red leaf lettuce (Lactuca sativa) cultivated under red LEDs (640 nm, 300 μmol m^{-2}s^{-1}) and far-red LEDs (730 nm, 20 μmol m^{-2}s^{-1}) gained more biomass but had reduced anthocyanin and antioxidant activity. In contrast, using red LEDs (640 nm, 270 μmol m^{-2}s^{-1}) and blue LEDs (440 nm, 30 μmol m^{-2}s^{-1}) enhanced anthocyanin levels, antioxidant capacity, and leaf area [68]. Additionally, green leaf lettuce (Lactuca sativa) exposed to red LEDs (638 nm, 210 μmol m^{-2}s^{-1}) with an HPS lamp (300 μmol m^{-2}s^{-1}) showed increases in phenolics (28.5 %), tocopherols (33.5 %), sugars (52.5 %), and antioxidant capacity (14.5 %) but lower vitamin C levels. Red LEDs (638 nm, 300 μmol m^{-2}s^{-1}) combined with an HPS lamp (90 μmol m^{-2}s^{-1}) increased nitrate concentration by 12.5 % in light green leaf lettuce but reduced it by 56.2 % in red leaf lettuce and 20.0 % in green leaf lettuce [69,70].

Fig. 9. Decay curves of Mn^{4+} emission ($\lambda_{ex.}$ = 330 nm, λ_{em} = 698 nm) in SrNaZrO$_3$: Mn^{4+} phosphors.

3.6.2. Chromaticity coordinate properties

The PL spectra obtained under 325 nm excitation for the five concentration-pair phosphor powders provide CIE chromaticity coordinates (x, y) values, as illustrated in Fig. 10. The calculated chromaticity coordinates can be found in Table 2. As the concentration of Mn increases, all chromaticity points shift towards the deep red region. The CIE coordinates (x, y) systematically change from (0.693, 0.307) to (0.707, 0.293) due to the redshift of PL. In comparison to the commercial red phosphor Y_2O_2S: Eu^{3+} (0.622, 0.351), the results obtained for the optimized phosphor in this study, including PL and CIE coordinates, closely align. However, they surpass the minimum red color coordinates specified by the National Television Standard Committee (NTSC) and other red phosphors, as referenced in Table 3. These findings affirm that $SrNaZrO_3$:Mn^{4+} operates as a highly efficient phosphor and has the potential to compete with established materials in solid-state lighting applications. Assessing the color purity of samples serves as a method for evaluating the overall luminescent properties of phosphors. The color purity equation is provided below:

$$\text{color purity} = \frac{\sqrt{(x - x_i)^2 + (y - y_i)^2}}{\sqrt{(x_d - x_i)^2 + (y_d - y_i)^2}} \times 100\% \quad (10)$$

In Eq. (7), x and y represent the coordinates of the sample we prepared. Meanwhile, $(x_d, y_d) = (0.735, 0.265)$ refer to the coordinates of the dominant emission wavelength, and $(x_i, y_i) = (0.310, 0.316)$ represents the coordinates of white illumination [71]. The calculated color purities of the samples, as per the provided formula, are additionally presented in Table 3. The outcomes confirm that these phosphor samples exhibit outstanding luminescent capabilities when applied in solid-state lighting.

To assess the Correlated Color Temperature (CCT), associated with the color appearance of the prepared nanophosphor powders, the McCamy empirical equation [72,73] was applied, as depicted below:

$$\text{CCT} = -449n^3 + 3525n^2 - 6823.3n + 5520.33. \quad (11)$$

where n is the inverse slope of the line defined by the chromaticity epicenter ($n = (x - x_e)/(y - y_e)$) with $x_e = 0.3320$ and $y_e = 0.1858$, the variables x and y represent the chromaticity coordinates of the sample. Table 3 displays the CCTs achieved for $SNaZrO_3$:Mn^{4+} at various concentrations, ranging from around 5463 K–6857 K. These values exceed the CCTs for soft white compact fluorescent and LED lamps. However, it is in the range of pure white and cool white light. The 5500

K pure white color is entirely neutral, devoid of any yellow or blue tint. It represents the purest form of white, appearing free from any discernible shade. This neutral light color lacks both yellow and blue undertones. Furthermore, the 5500 K light seamlessly complements other colors, effortlessly harmonizing with both cool and warm tones. The color temperature of 6000 K falls within the spectrum between white and blue on the graph, resulting in cool white light. Cool white LEDs not only enhance on-road visibility but also offer an exotic aftermarket appearance due to the bluish tint. Distinctions among 5000 K, 5500 K, and 6000 K LEDs become more apparent when these lights are compared side by side [36,74,75]. Consequently, $SrNaZrO_3$:Mn^{4+} phosphor exhibits intense and nearly pure red emission, hence, it emerges as a suitable material for LEDs and display lighting, whether utilized in conjunction with or without a green and blue LED chip.

3.7. Temperature sensing and thermal stability properties of $SrNaZrO_3$: Mn^{4+} phosphors

The thermal stability of phosphor materials is a key technological parameter required to ensure their ability to maintain luminescence efficiency and structural integrity under elevated temperatures during LED operation. This property is critical for delivering consistent light output and color quality, both of which are essential for the long-term performance and reliability of LEDs. At high temperatures, non-radiative relaxation processes may increase, resulting in reduced emission efficiency due to thermal quenching (heat-induced degradation). In LED applications, the PL intensity at 150 °C, relative to that at room temperature, is commonly used as a metric. To evaluate the thermal stability of these phosphors, temperature-dependent photoluminescence measurements were conducted (Fig. 11 (a and c)), and thermal quenching temperature metrics (T50) were used to identify the temperature at which luminescence drops by 50 % ($T_{1/2}$). These figures illustrate the temperature-dependent PL spectra of $SrNaZrO_3$:Mn^{4+} (Mn1 and Mn3 samples) under 325 nm He-Cd laser excitation. Similar to the room-temperature PL spectra in Fig. 8(B), the temperature-dependent spectra in Fig. 11(a) and (c) consistently exhibit Mn^{4+} absorption transition lines. As temperature increases, the integrated emission intensities of both blue and red emission lines decrease exponentially (Fig. 11(b) and (d)), while the peak positions remain unchanged. This decrease in emission intensity, known as thermal quenching, is primarily caused by enhanced nonradiative de-excitation processes within the nanocrystals, which dissipate excitation energy more rapidly at elevated temperatures. Temperature measurement is crucial across various fields, including scientific research, technological innovation, biomedical applications, and the management of industrial processes. Accurate analysis is essential for optimizing phosphor performance, particularly in applications such as thermographic luminescence temperature sensors and maintaining LED stability under varying thermal conditions.

For temperature sensing using the line broadening technique, only the 637 nm and 698 nm emission bands are considered in this study. The emission peaks at 423 nm and 698 nm are closely positioned, creating a distinct valley at 637 nm due to the overlap of these two peaks. As the temperature increases, the intensity ratio (I_{698}/I_{423}) of the red band relative to the blue band gradually decreases compared to the red emission band (see Fig. 12(a)). This behavior is attributed to the broadening of the FWHM and the reduction in emission intensity. Due to these unique thermal responses, the valley intensity at 637 nm and the peak intensity at 698 nm are suitable for ratiometric temperature sensing. Fig. 12(b) shows the variation in the I_{637}/I_{698} ratio with temperature, revealing a clear linear increase as temperature rises. The temperature-sensing behavior was analyzed using the valley-to-peak ratio (VPR) method. The VPR provided an improved linear fit, with R^2 values of 0.9975 and 0.9988 for Mn1 and Mn3, respectively. Thus, the relationship between the VPR of I_{637}/I_{698} and temperature can be effectively modeled using a linear function, as described in Equation
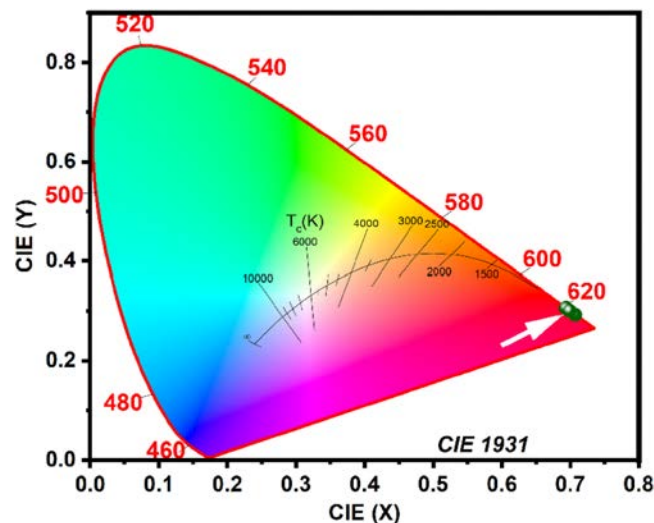

Fig. 10. The CIE chromaticity coordinates of $SrNaZrO_3$:Mn^{4+} phosphors.

Table 3
CIE coordinate, CCT and color purity of SrNaZrO$_3$:Mn^{4+} phosphors in comparison with other red phosphors.

Sample	CIE coordinates		CCT (K)	color purity (%)	Reference
	x	y			
NTSC	0.670	0.346	2967		[76]
ZnGeN$_2$:Mn^{2+}	0.630	0.370	1992		[77]
Y$_2$MoO$_6$:Eu^{3+}	0.654	0.353	2538		[78]
NaLa$_4$[Mo$_3$O$_{15}$]F:Eu^{3+}	0.663	0.333	3328		[79]
SrS:Eu^{2+}	0.626	0.373	1931	86	[80]
Ca$_9$Bi(VO$_4$)$_7$:$_{0.07}$Eu^{3+}	0.645	0.355		90	[81]
Ca$_9$Bi(VO$_4$)$_7$:$_{0.07}$Eu^{3+},$_{0.08}$Sm^{3+}	0.666	0.334		95	[81]
SrNaZrO$_3$:$_{0.01}$Mn^{4+}/Mn^{2+}	0.693	0.307	5463	90	This work
SrNaZrO$_3$:$_{0.03}$Mn^{4+}/Mn^{2+}	0.699	0.301	6047	91	This work
SrNaZrO$_3$:$_{0.05}$Mn^{4+}/Mn^{2+}	0.693	0.306	5528	90	This work
SrNaZrO$_3$:$_{0.07}$Mn^{4+}/Mn^{2+}	0.707	0.293	6857	93	This work
SrNaZrO$_3$:$_{0.09}$Mn^{4+}/Mn^{2+}	0.699	0.301	6058	91	This work
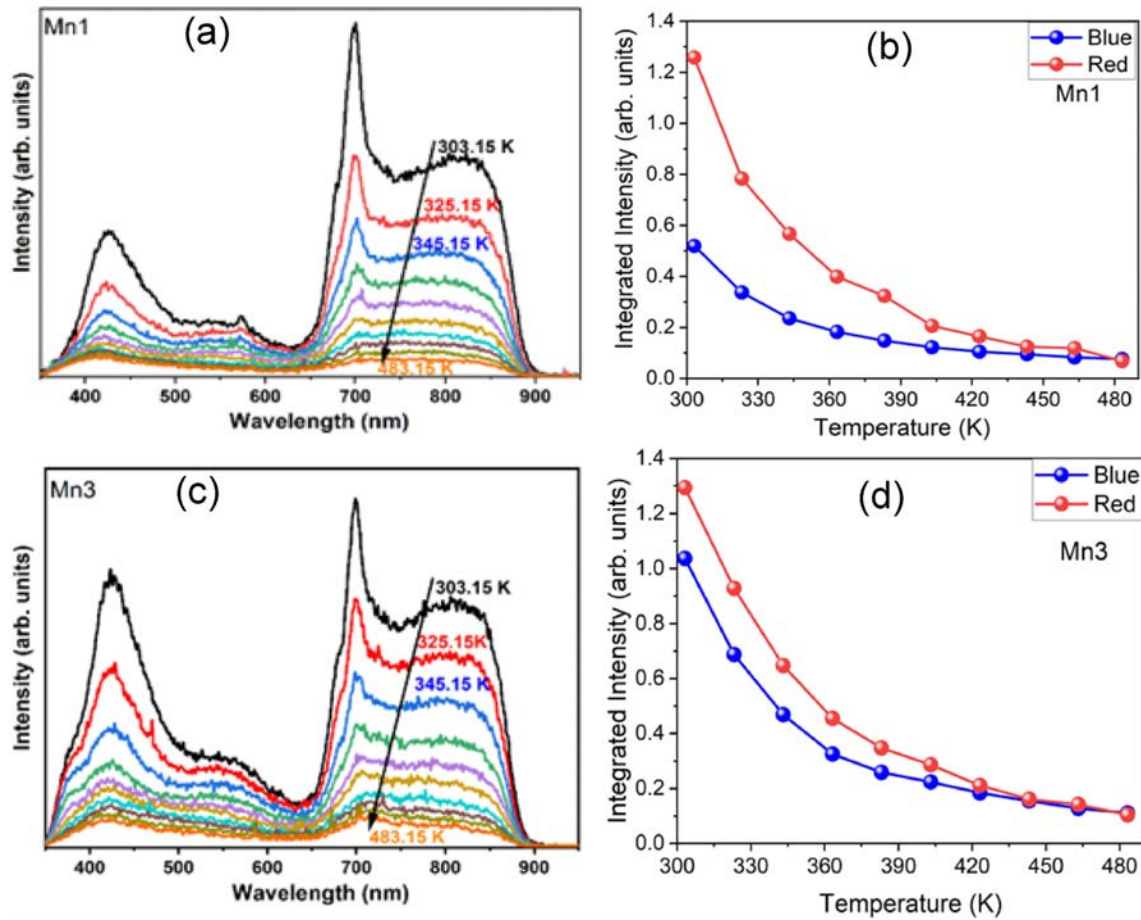
Fig. 11. Temperature dependence photoluminescence spectra of (a) Mn1, (b) Mn3, and the temperature quenching (c) Mn1, (d) Mn3 for the 637 and 698 nm respectively.

(12).

$$VPR = \Psi(T - T_0) + \varphi \qquad (12)$$

where Ψ represents the slope of the linear fit, φ is constant, and T_0 is the initial temperature.

To compare with various thermometric methods, the relative temperature sensing sensitivity crucial parameter (S_r) is assessed, representing the rate of change of the VPR at a particular temperature. The S_r can be computed using equation (13);

$$S_r = \left| \frac{1}{VPR} \frac{dVPR}{dT} \right| \qquad (13)$$

As depicted in Fig. 12(c), the maximum S_r value is ~2.49 % K^{-1} and ~0.64 % K^{-1} at 303.15 K. These are significantly better than other previously reported temperature sensors doped with Mn ions, such as: Na$_3$Sc$_2$P$_3$O$_{12}$:Eu^{2+},Mn^{2+} (1.556%K^{-1}) [82], Y$_3$Al$_5$O$_{12}$:Mn^{3+},Mn^{4+},Nd^{3+} (1.69%K^{-1}) [83], CaGdAlO$_4$:Mn^{4+},Tb^{3+} (2.3%K^{-1}) [84], SrGdLiTeO$_6$: Mn^{4+},Eu^{3+} (4.9%K^{-1}) [85], NaLaMgWO$_6$:Mn^{4+}/Eu^{3+} (0.86 %K^{-1}) [86], Y$_3$Al$_5$O$_{12}$:Mn^{3+},Mn^{4+},Nd^{3+} (0.54%K^{-1}) [87], NaBiF$_4$: Yb^{3+}/Er^{3+}/Mn^{2+} (0.559 %K^{-1}) [88], La$_2$LiSbO$_6$:Tb^{3+},Mn^{4+} (0.946%
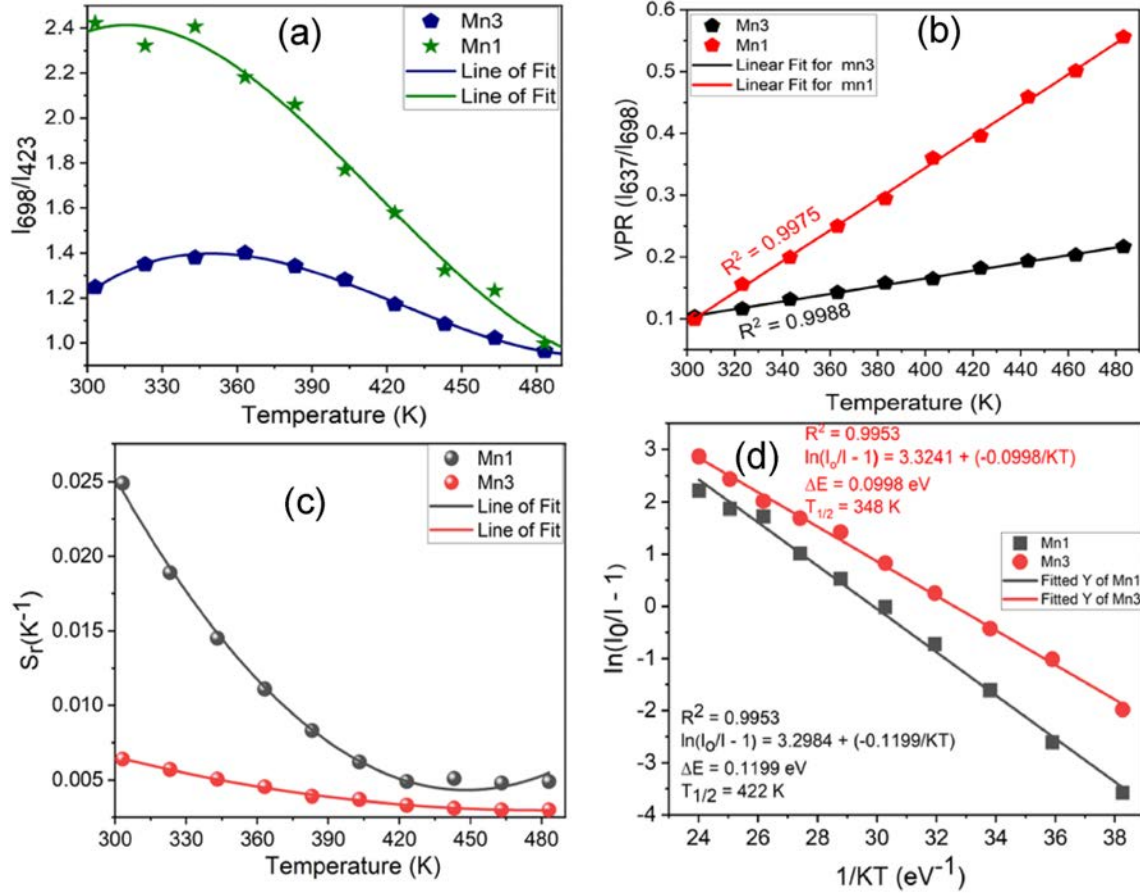
Fig. 12. (a) Intensity ratio variation plot (I_{698}/I_{438}) vs Temperature, (b) variation of VPR (I_{367}/I_{698}) as a function of temperature, (c) relative sensitivity (S_r) as a function of temperature, (d) plot of ($I_0/I - 1$) vs 1/KT, for Mn1 and Mn3 samples.

K^{-1}) [89], A_2LaNbO_6:Mn^{4+},Eu^{3+} (1.51%K^{-1}) [90]. With its high relative temperature sensitivity, $SrNaZrO_3$:0.01Mn^{4+} is exceptionally well-suited for use as a fluorescent temperature probe and optical thermometers.

Analyzing the thermal quenching temperature (T_Q) of $Sr_{0.9}Na_{0.2}Zr_{0.9}Mn_{0.1}O_3$ and $Sr_{0.9}Na_{0.2}Zr_{0.7}Mn_{0.3}O_3$ (referred to as Mn1 and Mn3 samples) phosphors above the maximum packaging temperature of 420 K is crucial. To achieve this, the spectral emission intensities within the 300–470 K range were integrated and normalized. The resulting emission intensity data, I(T), was then modeled using the Fermi-Dirac distribution function, and the variation in emission intensities was further described using the Arrhenius equation [91,92]:

$$I = \frac{I_0}{1 + Be^{-\Delta E/KT}} \tag{14}$$

$$I \Big/ I_0 - 1 = \sum_{n=1}^{N} B_n \exp.(-\Delta E_n / KT) \tag{15}$$

where, I_0 and I represent the integrated emission intensities from the 3 d^3 state of Mn^{4+} at low and high temperatures, respectively. B_n is a constant, ΔE_n represents the activation energy for thermal quenching, and K is the Boltzmann's constant. The plot of $\ln(I_0/ I - 1)$ vs K^{-1} in Fig. 12. (d) aligns well with the single Arrhenius function when N = 1. The linear fitting formula used for modeling at higher temperatures is expressed as follows:

$$\ln\left(\frac{I_0}{I} - 1\right) = \frac{\Delta E_n}{K} \cdot \frac{1}{T} + \ln(B_n) \tag{16}$$

$$\left(\frac{I_0}{I} - 1\right) = 27.0693 \, exp\left(\frac{0.1199 \, eV}{KT}\right) \text{ for Mn1} \tag{17}$$

$$\left(\frac{I_0}{I} - 1\right) = 27.7739 \, exp\left(\frac{0.0998 \, eV}{KT}\right) \text{ for Mn3} \tag{18}$$

The temperature at which the integrated emission intensity of the Mn1 and Mn3 phosphors decreases to 50 % ($T_{1/2}$) of the intensity at room temperature was determined using Equation (19):

$$T_{1/2} = \frac{-\Delta E}{K \times \ln\left(\frac{1}{B}\right)} \tag{19}$$

The calculated results indicated 50 % quenching temperatures of 422 K and 348 K for the Mn1 and Mn3 samples, respectively. The low $T_{1/2}$ value observed for the Mn3 sample is attributed to thermal quenching and concentration quenching, as discussed in detail in Section 3.5. This demonstrates that the $SrNaZrO_3$:Mn^{4+} phosphor exhibits excellent thermal stability, making it suitable for LED applications such as automotive lighting, outdoor illumination, and high-power devices. However, the Mn1 and Mn3 phosphor samples exhibit low quantum yields (QY) of 0.09 % and 0.05 %, respectively, as illustrated in Fig. S1 (Supplementary).

4. Conclusions

In summary, $SrNaZrO_3$:Mn^{4+} was synthesized through a sol-gel reaction and subjected to characterization using various techniques, including x-ray diffraction (XRD), field emission scanning electron

microscopy (FESEM), high-resolution transmission electron microscopy (HRTEM), diffuse reflectance absorbance (DRA), spectro-fluorophotometry, and x-ray photoelectron spectroscopy (XPS). These analyses were conducted to investigate the structural, morphological, and photoluminescent (PL) properties of the material. The particle size falls within the nanometer range, ranging from 20 nm to 63 nm, displaying an inhomogeneous structure. Rietveld results conclude that Mn^{4+} ion occupies the Zr 4a site instead of the Sr 4c site. The six-fold 4a site suffers an oxidation-state change that induces a reduction in the Mn-O bond length, resulting in a slight reduction of the red-emission intensity with a systematic increase in the blue emission. All of the above is promoted by the $V_o^{\bullet\bullet}$. The determined optical band gap ranges from 1.86 eV to 2.22 eV. The photoluminescence intensity of the $SrNaZrO_3$: Mn^{4+} nanophosphor decreases consistently with increasing Mn^{4+} concentration, both at room temperature and high temperatures (303.15–483.15 K), due to exchange interaction quenching. The phosphor demonstrates excellent thermal stability, retaining half its emission intensity at 422 K and exhibiting a thermal relative sensitivity of 2.9 % K^{-1}. With CIE chromaticity coordinates close to standard red emitters and a red-light purity of 90–93 %, it is well-suited for use as a red-light component in LED development, owing to its strong red emission and high temperature stability

CRediT authorship contribution statement

A. Nathan-Abutu: Writing – original draft, Validation, Methodology, Investigation, Data curation. **I. Ahemen:** Writing – review & editing, Formal analysis, Data curation, Conceptualization. **R.E. Kroon:** Writing – review & editing, Investigation, Formal analysis, Data curation. **L.J.B. Erasmus:** Investigation, Methodology. **A. Ramirez-Dela-Cruz:** Validation, Investigation. **A. Reyes-Rojas:** Writing – review & editing, Validation, Supervision, Resources, Project administration, Methodology, Investigation, Formal analysis, Data curation, Conceptualization.

Declaration of competing interest

The authors declare that they do not have any identifiable conflicting financial interests or personal connections that might have seemed to impact the research presented in this article.

Acknowledgement

Appendix A. Supplementary data

Supplementary data to this article can be found online at https://doi.org/10.1016/j.jlumin.2024.121030.

Data availability

Data will be made available on request.

References

[1] S. Ray, J. Rawat, A review on the exploration of the red phosphors for the fabrication of phosphor-converted-LEDs for plant growth in indoor farming, ECS Trans. 107 (2022) 20091–20100, https://doi.org/10.1149/10701.20091ecst.

[2] W. Wang, X. Yang, S. Xiao, $Ba_3Y_2WO_9$:Mn^{4+}: a near-UV and yellow-green light excited red phosphor for greenhouse cultivation, J. Lumin. 225 (2020) 117406, https://doi.org/10.1016/j.jlumin.2020.117406.

[3] T. Polívka, H.A. Frank, Molecular factors controlling photosynthetic light harvesting by carotenoids, Acc. Chem. Res. 43 (2010) 1125–1134, https://doi.org/10.1021/ar100030m.

[4] A.J. Simkin, L. Kapoor, C.G.P. Doss, T.A. Hofmann, T. Lawson, S. Ramamoorthy, The role of photosynthesis related pigments in light harvesting, photoprotection and enhancement of photosynthetic yield in planta, Photosynth. Res. 152 (2022) 23–42, https://doi.org/10.1007/s11120-021-00892-6.

[5] H. Lokstein, G. Renger, J. Götze, Photosynthetic light-harvesting (antenna) complexes—structures and functions, Molecules 26 (2021) 3378, https://doi.org/10.3390/molecules26113378.

[6] T. Mirkovic, E.E. Ostroumov, J.M. Anna, R. van Grondelle, Govindjee, G.D. Scholes, Light absorption and energy transfer in the antenna complexes of photosynthetic organisms, Chem. Rev. 117 (2017) 249–293, https://doi.org/10.1021/acs.chemrev.6b00002.

[7] T.W. Tibbitts, D.C. Morgan, I.J. Warrington, Growth of lettuce, spinach, mustard, and wheat plants under four combinations of high-pressure sodium, metal halide, and tungsten halogen lamps at equal PPFD, J. Am. Soc. Hortic. Sci. 108 (1983) 622–630, https://doi.org/10.21273/JASHS.108.4.622.

[8] I. Monostori, M. Heilmann, G. Kocsy, M. Rakszegi, M. Ahres, S.B. Altenbach, G. Szalai, M. Pál, D. Toldi, L. Simon-Sarkadi, N. Harnos, G. Galiba, É. Darko, LED lighting – modification of growth, metabolism, yield and flour composition in wheat by spectral quality and intensity, Front. Plant Sci. 9 (2018) https://doi.org/10.3389/fpls.2018.00605.

[9] M. Al Murad, K. Razi, B.R. Jeong, P.M.A. Samy, S. Muneer, Light emitting diodes (LEDs) as agricultural lighting: impact and its potential on improving physiology, flowering, and secondary metabolites of crops, Sustainability 13 (2021) 1985, https://doi.org/10.3390/su13041985.

[10] C.-C. Hsieh, Y.-H. Li, C.-C. Hung, Modular design of the LED vehicle projector headlamp system, Appl. Opt. 52 (2013) 5221, https://doi.org/10.1364/AO.52.005221.

[11] G. Blasse, B.C. Grabmaier, A general introduction to luminescent materials, in: Luminescent Materials, Springer Berlin Heidelberg, Berlin, Heidelberg, 1994, pp. 1–9, https://doi.org/10.1007/978-3-642-79017-1_1.

[12] B. Lei, Y. Liu, Z. Ye, C. Shi, Luminescence properties of $CdSiO_3$:Mn^{2+} phosphor, J. Lumin. 109 (2004) 215–219, https://doi.org/10.1016/j.jlumin.2004.02.010.

[13] M.H. Du, Chemical trends of Mn^{4+} emission in solids, J. Mater. Chem. C 2 (2014) 2475–2481, https://doi.org/10.1039/C4TC00031E.

[14] T. Hasegawa, Y. Nishiwaki, F. Fujishiro, S. Kamei, T. Ueda, Quantitative determination of the effective Mn^{4+} concentration in a Li_2TiO_3:Mn^{4+} phosphor and its effect on the photoluminescence efficiency of deep red emission, ACS Omega 4 (2019) 19856–19862, https://doi.org/10.1021/acsomega.9b02798.

[15] L. Shi, D. Zhao, R. Zhang, Q. Yao, W. Liu, A new optical temperature sensor based on the fluorescence intensity ratio of Mn^{2+} and Mn^{4+}, J. Am. Ceram. Soc. 105 (2022) 7479–7491, https://doi.org/10.1111/jace.18698.

[16] A. Nathan-Abutu, I. Ahemen, A. Reyes-Rojas, Structural and optical investigation of novel $Sr_{1-x}Na_{2x}ZrO_3$ perovskite nanoparticles, Phys. B Condens. Matter 653 (2023) 414655, https://doi.org/10.1016/j.physb.2023.414655.

[17] A. Nathan-Abutu, I. Ahemen, R.E. Kroon, A. Reyes-Rojas, Downshifting photoluminescence of Erbium doped $NaSrZrO_3$ for solid-state lighting, J. Alloys Compd. 987 (2024) 174104, https://doi.org/10.1016/j.jallcom.2024.174104.

[18] A. Nathan-Abutu, D. Lardizabal-Gutierrez, A. Reyes-Rojas, Evidence of novel crystal structure in cesium-doped sodium zirconate perovskite and its impact on optical and CO_2 sorption properties, J. Nanoparticle Res. 26 (2024) 109, https://doi.org/10.1007/s11051-024-06019-x.

[19] R.D. Shannon, Revised effective ionic radii and systematic studies of interatomic distances in halides and chalcogenides, Acta Crystallogr. A 32 (1976) 751–767, https://doi.org/10.1107/S0567739476001551.

[20] Jun Ho Kim, Jeong Woo Yun, Sulfur tolerance effects on $Sr_{0.92}Y_{0.08}Ti_{0.5}Fe_{0.5}O_{3-\delta}$ as an alternative anode in solid oxide fuel cells,, J. Electrochem. Sci. Technol 9 (2018) 133–140, https://doi.org/10.5229/JECST.2018.9.2.133.

[21] Y.Q. Jia, Crystal radii and effective ionic radii of the rare earth ions, J. Solid State Chem. 95 (1991) 184–187, https://doi.org/10.1016/0022-4596(91)90388-X.

[22] A. Nathan, J. Rex, A. Roy, Luminescence characteristics of polymer passivated strontium aluminate phosphor, Physical Science International Journal 8 (2015) 1–6, https://doi.org/10.9734/PSIJ/2015/20601.

[23] O. Kalu, A.N. Abutu, H. Esparza Ponce, A. Ramirez-DelaCruz, R.E. Kroon, A. Reyes-Rojas, Structural and optical characterization of RF sputtered CdMgZnO thin film with different Cd concentrations, Mater. Chem. Phys. 308 (2023) 128314, https://doi.org/10.1016/j.matchemphys.2023.128314.

[24] Q. Tian, L. Zhang, J. Liu, N. Li, Q. Ma, J. Zhou, Y. Sun, Synthesis of MoS_2/$SrZrO_3$ heterostructures and their photocatalytic H_2 evolution under UV irradiation, RSC Adv. 5 (2015) 734–739, https://doi.org/10.1039/C4RA11135D.

[25] N. Bibi, M.Z. Hussain, S. Hussain, S. Ahmed, I. Ahmad, S. Zhang, A. Iqbal, Excellent electrochemical performance of $SrZrO_3$ nanorods as supercapacitor electrode in aqueous electrolytes, Appl. Surf. Sci. 495 (2019) 143587, https://doi.org/10.1016/j.apsusc.2019.143587.

[26] M. Miodyńska, B. Bajorowicz, P. Mazierski, W. Lisowski, T. Klimczuk, M.J. Winiarski, A. Zaleska-Medynska, J. Nadolna, Preparation and photocatalytic

properties of BaZrO$_3$ and SrZrO$_3$ modified with Cu$_2$O/Bi$_2$O$_3$ quantum dots, Solid State Sci. 74 (2017) 13–23, https://doi.org/10.1016/j.solidstatesciences.2017.10.003.

[27] H.W. Nesbitt, D. Banerjee, Interpretation of XPS Mn(2p) spectra of Mn oxyhydroxides and constraints on the mechanism of MnO$_2$ precipitation, Am. Mineral. 83 (1998) 305–315, https://doi.org/10.2138/am-1998-3-414.

[28] S. Nemrava, D.A. Vinnik, Z. Hu, M. Valldor, C.-Y. Kuo, D.A. Zherebtsov, S. A. Gudkova, C.-T. Chen, L.H. Tjeng, R. Niewa, Three oxidation states of manganese in the barium hexaferrite BaFe$_{12-x}$Mn$_x$O$_{19}$, Inorg. Chem. 56 (2017) 3861–3866, https://doi.org/10.1021/acs.inorgchem.6b02688.

[29] N.A. Zaitseva, T.A. Onufrieva, J.A. Barykina, T.I. Krasnenko, E.V. Zabolotskaya, R. F. Samigullina, Magnetic properties and oxidation states of manganese ions in doped phosphor Zn$_2$SiO$_4$:Mn, Mater. Chem. Phys. 209 (2018) 107–111, https://doi.org/10.1016/j.matchemphys.2018.01.071.

[30] S. Jiang, Z. You, N. Tang, Effects of calcination temperature and calcination atmosphere on the performance of Co$_3$O$_4$ catalysts for the catalytic oxidation of toluene, Processes 11 (2023) 2087, https://doi.org/10.3390/pr11072087.

[31] I. Morad, X. Liu, J. Qiu, Crystallization-induced valence state change of Mn^{2+} → Mn^{4+} in LiNaGe$_4$O$_9$ glass-ceramics, J. Am. Ceram. Soc. 103 (2020) 3051–3059, https://doi.org/10.1111/jace.17006.

[32] A.Y. Madkhli, Simultaneous oxidation of Mn^{2+} to Mn^{4+} by devitrification of transparent glassy Na$_2$Ge$_4$O$_9$: Mn, Ceram. Int. 50 (2024) 24913–24920, https://doi.org/10.1016/j.ceramint.2023.12.170.

[33] L. Shi, D. Zhao, R. Zhang, Q. Yao, W. Liu, A new optical temperature sensor based on the fluorescence intensity ratio of Mn^{2+} and Mn^{4+}, J. Am. Ceram. Soc. 105 (2022) 7479–7491, https://doi.org/10.1111/jace.18698.

[34] C. Ragoen, L. Cormier, A.-I. Bidegaray, S. Vives, F. Henneman, N. Trcera, S. Godet, A XANES investigation of the network-modifier cations environment before and after the Na$^+$/K$^+$ ion-exchange in silicate glasses, J. Non-Cryst. Solids 479 (2018) 97–104, https://doi.org/10.1016/j.jnoncrysol.2017.10.021.

[35] J.M. Rimsza, R.E. Jones, Inelastic relaxation processes in amorphous sodium silicates, J. Am. Ceram. Soc. 107 (2024) 1883–1894, https://doi.org/10.1111/jace.19435.

[36] Y.-F. Huang, Y.-C. Chi, M.-K. Chen, D.-P. Tsai, D.-W. Huang, G.-R. Lin, Red/green/blue LD mixed white-light communication at 6500K with divergent diffuser optimization, Opt Express 26 (2018) 23397, https://doi.org/10.1364/OE.26.023397.

[37] R. López, R. Gómez, Band-gap energy estimation from diffuse reflectance measurements on sol–gel and commercial TiO2: a comparative study, J. Sol. Gel Sci. Technol. 61 (2012) 1–7, https://doi.org/10.1007/s10971-011-2582-9.

[38] Y.S. Malghe, U.C. Yadav, Synthesis, characterization and investigation of dielectric properties of nanosized SrZrO$_3$, J. Therm. Anal. Calorim. 122 (2015) 589–594, https://doi.org/10.1007/s10973-015-4804-9.

[39] P.R. Jubu, O.S. Obaseki, A. Nathan-Abutu, F.K. Yam, Y. Yusof, M.B. Ochang, Dispensability of the conventional Tauc's plot for accurate bandgap determination from UV–vis optical diffuse reflectance data, Results in Optics 9 (2022) 100273, https://doi.org/10.1016/j.rio.2022.100273.

[40] A.A. Azab, E.E. Ateia, S.A. Esmail, Comparative study on the physical properties of transition metal-doped (Co, Ni, Fe, and Mn) ZnO nanoparticles, Appl. Phys. A 124 (2018) 469, https://doi.org/10.1007/s00339-018-1871-3.

[41] V.M. Igba, I. Ahemen, A.N. Amah, F.B. Dejene, R. Sha'Ato, A. Reyes-Rojas, J. A. Duarte-Moller, J.R. Parra-Michel, Structural elucidation and optical properties of LiZrO$_2$ –LiBaZrO$_3$ nanocomposite doped with Mn^{2+} ions, Opt. Mater. Express 10 (2020) 2877, https://doi.org/10.1364/OME.402111.

[42] V. Đorđević, M.G. Brik, A.M. Srivastava, M. Medić, P. Vulić, E. Glais, B. Viana, M. D. Dramićanin, Luminescence of Mn4+ ions in CaTiO$_3$ and MgTiO$_3$ perovskites: relationship of experimental spectroscopic data and crystal field calculations, Opt. Mater. 74 (2017) 46–51, https://doi.org/10.1016/j.optmat.2017.03.021.

[43] A.M. Srivastava, M.G. Brik, Ab initio and crystal field studies of the Mn^{4+}-doped Ba$_2$LaNbO$_6$ double-perovskite, J. Lumin. 132 (2012) 579–584, https://doi.org/10.1016/j.jlumin.2011.09.017.

[44] D.P. R, P.U.W.L. B, G.H.E. Boulanger, Magnetic field effect and dynamical Jahn-teller effect on a 4T1 level of a d5 ion coupled to ε-vibrational modes, Phys. Status Solidi 213 (1999) 79–91.

[45] M.K. Kretov, I.M. Iskandarova, B.V. Potapkin, A.V. Scherbinin, A.M. Srivastava, N. F. Stepanov, Simulation of structured 4T1→6A1 emission bands of Mn^{2+} impurity in Zn$_2$SiO$_4$: a first-principle methodology, J. Lumin. 132 (2012) 2143–2150, https://doi.org/10.1016/j.jlumin.2012.03.067.

[46] R. Belbal, L. Gacem, B. Bentria, B. Saidat, M.T. Soltani, L. Guerbous, Preparation and luminescence properties of novel K$_2$ZnP$_2$O$_7$: Mn^{2+} green phosphor, J. Mater. Sci. Mater. Electron. 32 (2021) 27475–27483, https://doi.org/10.1007/s10854-021-07123-7.

[47] M.H. Cho, Y.S. Lee, Electronic structure and red emission of Mn-ion-doped SrZrO$_3$, J. Kor. Phys. Soc. 64 (2014) 1866–1871, https://doi.org/10.3938/jkps.64.1866.

[48] Y. Dou, Equations for calculating Dq and B, J. Chem. Educ. 67 (1990) 134, https://doi.org/10.1021/ed067p134.

[49] K. Li, D. Zhu, R. Van Deun, Photoluminescence properties and crystal field analysis of a novel red-emitting phosphor K$_2$BaGe$_8$O$_{18}$:Mn^{4+}, Dyes Pigments 142 (2017) 69–76, https://doi.org/10.1016/j.dyepig.2017.03.007.

[50] A.M. Srivastava, M.G. Brik, S.J. Camardello, H.A. Comanzo, F. Garcia-Santamaria, Optical spectroscopy and crystal field studies of the Mn^{4+} ion (3d^3) in the double perovskite NaLaMgTeO$_6$, Z. Naturforsch. B Chem. Sci. 69 (2014) 141–149, https://doi.org/10.5560/znb.2014-3259.

[51] Z. Bryknar, V. Trepakov, Z. Potůček, L. Jastrabík, Luminescence spectra of SrTiO$_3$: Mn^{4+}, J. Lumin. 87–89 (2000) 605–607, https://doi.org/10.1016/S0022-2313(99)00325-7.

[52] X.-X. Wu, W. Fang, W.-L. Feng, W.-C. Zheng, Electron paramagnetic resonance parameters of Mn^{4+} ion in h-BaTiO$_3$ crystal from a two-mechanism model, Pramana 72 (2009) 569–575, https://doi.org/10.1007/s12043-009-0050-7.

[53] A. Srivastava, M.G. Brik, Systematic crystal field studies of Mn^{4+} -doped perovskites, ECS Meeting Abstracts MA2013-02 (2013), https://doi.org/10.1149/MA2013-02/49/2719, 2719–2719.

[54] M.G. Brik, A.M. Srivastava, Electronic energy levels of the Mn^{4+} ion in the perovskite, CaZrO$_3$, ECS Journal of Solid-State Science and Technology 2 (2013) R148–R152, https://doi.org/10.1149/2.020307jss.

[55] Y. Sun, P. Li, Z. Wang, J. Cheng, Z. Li, C. Wang, M. Tian, Z. Yang, Tunable emission phosphor Ca$_{0.75}$Sr$_{0.2}$Mg$_{1.05}$(Si$_2$O$_6$):Eu^{2+}, Mn^{2+} : luminescence and mechanism of host, energy transfer of Eu^{2+}→ Mn^{2+}, Eu^{2+} → host, and host → Mn^{2+}, J. Phys. Chem. C 120 (2016) 20254–20264, https://doi.org/10.1021/acs.jpcc.6b05993.

[56] J. Grigorjevaite, E. Ezerskyte, J. Páterek, S. Saitzek, A. Zabiliūtė-Karaliūnė, P. Vitta, D. Enseling, T. Jüstel, A. Katelnikovas, Luminescence and luminescence quenching of K$_2$Bi(PO$_4$)(MoO$_4$):Sm^{3+} phosphors for horticultural and general lighting applications, Mater Adv 1 (2020) 1427–1438, https://doi.org/10.1039/D0MA00369G.

[57] N. Lu, T. Maruo, M. Johkan, M. Hohjo, S. Tsukagoshi, Y. Ito, T. Ichimura, Y. Shinohara, Effects of supplemental lighting with light-emitting diodes (LEDs) on tomato yield and quality of single-truss tomato plants grown at high planting density, Environ. Control Biol. 50 (2012) 63–74, https://doi.org/10.2525/ecb.50.63.

[58] K. Nanya, Y. Ishigami, S. Hikosaka, E. Goto, Effects of blue and red light on stem elongation and flowering of tomato seedlings, Acta Hortic. (2012) 261–266, https://doi.org/10.17660/ActaHortic.2012.956.29.

[59] C.S. Brown, A.C. Schuerger, J.C. Sager, Growth and photomorphogenesis of pepper plants under red light-emitting diodes with supplemental blue or far-red lighting, J. Am. Soc. Hortic. Sci. 120 (1995) 808–813, https://doi.org/10.21273/JASHS.120.5.808.

[60] H. Li, C. Tang, Z. Xu, X. Liu, X. Han, Effects of different light sources on the growth of non-heading Chinese cabbage (Brassica campestris L.), J. Agric. Sci. 4 (2012), https://doi.org/10.5539/jas.v4n4p262.

[61] T. Mizuno, W. Amaki, H. Watanabe, Effects of monochromatic light irradiation by led on the growth and anthocyanin contents in leaves of cabbage seedlings, Acta Hortic. (2011) 179–184, https://doi.org/10.17660/ActaHortic.2011.907.25.

[62] I. Tarakanov, O. Yakovleva, I. Konovalova, G. Paliutina, A. Anisimov, Light-emitting diodes: on the way to combinatorial lighting technologies for basic research and crop production, Acta Hortic. (2012) 171–178, https://doi.org/10.17660/ActaHortic.2012.956.17.

[63] M.G. Lefsrud, D.A. Kopsell, C.E. Sams, Irradiance from distinct wavelength light-emitting diodes affect secondary metabolites in kale, Hortscience 43 (2008) 2243–2244, https://doi.org/10.21273/HORTSCI.43.7.2243.

[64] Z. Bliznikas, A. Zukauskas, G. Samuolienė, A. Viršilė, A. Brazaitytė, J. Jankauskienė, P. Duchovskis, A. Novičkovas, Effect of supplementary pre-harvest led lighting on the antioxidant and nutritional properties of green vegetables, Acta Hortic. (2012) 85–91, https://doi.org/10.17660/ActaHortic.2012.939.10.

[65] G. Samuolienė, A. Urbonavičiūtė, P. Duchovskis, Z. Bliznikas, P. Vitta, A. Žukauskas, Decrease in nitrate concentration in leafy vegetables under a solid-state illuminator, Hortscience 44 (2009) 1857–1860, https://doi.org/10.21273/HORTSCI.44.7.1857.

[66] Q. Li, C. Kubota, Effects of supplemental light quality on growth and phytochemicals of baby leaf lettuce, Environ. Exp. Bot. 67 (2009) 59–64, https://doi.org/10.1016/j.envexpbot.2009.06.011.

[67] A. Zukauskas, Z. Bliznikas, K. Breivė, A. Novičkovas, G. Samuolienė, A. Urbonavičiūtė, A. Brazaitytė, J. Jankauskienė, P. Duchovskis, Effect of supplementary pre-harvest led lighting on the antioxidant properties of lettuce cultivars, Acta Hortic. (2011) 87–90, https://doi.org/10.17660/ActaHortic.2011.907.8.

[68] G.W. Stutte, S. Edney, T. Skerritt, Photoregulation of bioprotectant content of red leaf lettuce with light-emitting diodes, Hortscience 44 (2009) 79–82, https://doi.org/10.21273/HORTSCI.44.1.79.

[69] G.S. R, B.A.V. A, D.P. Samuoliene, Supplementary red-LED lighting and the changes in phytochemical content of two baby leaf lettuce varieties during three seasons, J. Food Agric. Environ. 10 (2012) 701–706.

[70] G. Samuolien, A. Brazaityte, R. Sirtautas, A. Novickovas, P. Duchovskis, Supplementary red-LED lighting affects phytochemicals and nitrate of baby leaf lettuce, J. Food Agric. Environ. 9 (2011) 271–274.

[71] Y. Qin, Q. Zeng, S. Chen, Z. Min, C. Yao, Synthesis and luminescent properties of Mn^{4+}-doped Li$_{2.06}$Nb$_{0.18}$Ti$_{0.76}$O$_3$ high color purity red-emission phosphor, J. Lumin. 257 (2023) 119757, https://doi.org/10.1016/j.jlumin.2023.119757.

[72] C.S. McCamy, Correlated color temperature as an explicit function of chromaticity coordinates, Color Res. Appl. 17 (1992) 142–144, https://doi.org/10.1002/col.5080170211.

[73] A. Nathan-Abutu, I. Ahemen, R.E. Kroon, A. Reyes-Rojas, Spectroscopic properties of red-emitting Sr$_{0.9}$Na$_{0.2}$ZrO$_3$:Eu^{3+} phosphors with potential applications in lasers and LEDs, Opt. Mater. 157 (2024) 116338, https://doi.org/10.1016/j.optmat.2024.116338.

[74] C.-C. Sun, C.-Y. Chen, C.-C. Chen, C.-Y. Chiu, Y.-N. Peng, Y.-H. Wang, T.-H. Yang, T.-Y. Chung, C.-Y. Chung, High uniformity in angular correlated-color-temperature distribution of white LEDs from 2800K to 6500K, Opt Express 20 (2012) 6622, https://doi.org/10.1364/OE.20.006622.

[75] M. te Kulve, L. Schlangen, L. Schellen, J.L. Souman, W. van Marken Lichtenbelt, Correlated colour temperature of morning light influences alertness and body

temperature, Physiol. Behav. 185 (2018) 1–13, https://doi.org/10.1016/j.physbeh.2017.12.004.

[76] P. Arsenyan, A. Petrenko, K. Leitonas, D. Volyniuk, J. Simokaitiene, T. Klinavičius, E. Skuodis, J.-H. Lee, J.V. Gražulevičius, Synthesis and performance in OLEDs of selenium-containing phosphorescent emitters with red emission color deeper than the corresponding NTSC standard, Inorg. Chem. 58 (2019) 10174–10183, https://doi.org/10.1021/acs.inorgchem.9b01283.

[77] M. Shang, J. Wang, J. Fan, H. Lian, Y. Zhang, J. Lin, $ZnGeN_2$ and $ZnGeN_2:Mn^{2+}$ phosphors: hydrothermal-ammonolysis synthesis, structure and luminescence properties, J Mater Chem C Mater 3 (2015) 9306–9317, https://doi.org/10.1039/C5TC01864A.

[78] K. Deng, T. Gong, Y. Chen, C. Duan, M. Yin, Efficient red-emitting phosphor for near-ultraviolet-based solid-state lighting, Opt Lett 36 (2011) 4470, https://doi.org/10.1364/OL.36.004470.

[79] S. Qi, H. Xie, Y. Huang, S. Il Kim, H.J. Seo, A narrow red-emitting phosphor of $NaLa_4[Mo_3O_{15}]F:Eu^{3+}$ with broad excitation band extending in blue wavelength region, Opt. Mater. Express 4 (2014) 190, https://doi.org/10.1364/OME.4.000190.

[80] J.-M. Kim, K.-N. Kim, J.-K. Park, C.-H. Kim, H.-G. Jang, Synthesis and luminescence characteristics of $SrS:Eu^{2+}$ red phosphor, J. Kor. Chem. Soc. 49 (2005) 138–144, https://doi.org/10.5012/jkcs.2005.49.2.138.

[81] Y. Wu, K. Qiu, W. Zhang, Q. Tang, Synthesis and luminescence enhancement of Eu^{3+}/Sm^{3+} co-doped $Ca_9Bi(VO_4)_7$ phosphor for white-light-emitting diodes, J. Mater. Sci. Mater. Electron. 30 (2019) 3045–3054, https://doi.org/10.1007/s10854-018-00583-4.

[82] X. Zhang, Z. Zhu, Z. Guo, Z. Sun, Y. Chen, A ratiometric optical thermometer with high sensitivity and superior signal discriminability based on $Na_3Sc_2P_3O_{12}: Eu^{2+}, Mn^{2+}$ thermochromic phosphor, Chem. Eng. J. 356 (2019) 413–422, https://doi.org/10.1016/j.cej.2018.09.075.

[83] K. Trejgis, L. Marciniak, The influence of manganese concentration on the sensitivity of bandshape and lifetime luminescent thermometers based on $Y_3Al_5O_{12}:Mn^{3+},Mn^{4+},Nd^{3+}$ nanocrystals, Phys. Chem. Chem. Phys. 20 (2018) 9574–9581, https://doi.org/10.1039/C8CP00558C.

[84] Y. Fang, Y. Zhang, Y. Zhang, J. Hu, Achieving high thermal sensitivity from ratiometric $CaGdAlO_4:Mn^{4+},Tb^{3+}$ thermometers, Dalton Trans. 50 (2021) 13447–13458, https://doi.org/10.1039/D1DT02185K.

[85] L. Li, G. Tian, Y. Deng, Y. Wang, Z. Cao, F. Ling, Y. Li, S. Jiang, G. Xiang, X. Zhou, Constructing ultra-sensitive dual-mode optical thermometers: utilizing FIR of Mn^{4+}/Eu^{3+} and lifetime of Mn^{4+} based on double perovskite tellurite phosphor, Opt Express 28 (2020) 33747, https://doi.org/10.1364/OE.409242.

[86] H. Zhou, N. Guo, M. Zhu, J. Li, Y. Miao, B. Shao, Photoluminescence and ratiometric optical thermometry in Mn^{4+}/Eu^{3+} dual-doped phosphor via site-favorable occupation, J. Lumin. 224 (2020) 117311, https://doi.org/10.1016/j.jlumin.2020.117311.

[87] K. Trejgis, L. Marciniak, The influence of manganese concentration on the sensitivity of bandshape and lifetime luminescent thermometers based on $Y_3Al_5O_{12}:Mn^{3+},Mn^{4+},Nd^{3+}$ nanocrystals, Phys. Chem. Chem. Phys. 20 (2018) 9574–9581, https://doi.org/10.1039/C8CP00558C.

[88] Y. Guo, J. Xie, M. Yu, W. Huang, H. Yang, X. Li, L. Wang, Q. Zhang, The enhanced up-conversion green by Yb-Mn dimer in $NaBiF_4:Yb^{3+}/Er^{3+}/Mn^{2+}$ for optical fiber temperature sensor, J. Alloys Compd. 888 (2021) 161497, https://doi.org/10.1016/j.jallcom.2021.161497.

[89] Y. Song, N. Guo, J. Li, Y. Xin, W. Lü, Y. Miao, Dual-emissive Ln^{3+}/Mn^{4+} Co-doped double perovskite phosphor via site-beneficial occupation, Mater Adv 2 (2021) 1402–1412, https://doi.org/10.1039/D0MA00841A.

[90] P. Wang, J. Mao, L. Zhao, B. Jiang, C. Xie, Y. Lin, F. Chi, M. Yin, Y. Chen, Double perovskite $A_2LaNbO_6:Mn^{4+},Eu^{3+}$ (A = Ba, Ca) phosphors: potential applications in optical temperature sensing, Dalton Trans. 48 (2019) 10062–10069, https://doi.org/10.1039/C9DT01524H.

[91] I. Ahemen, F.B. Dejene, R. Botha, Strong green-light emitting Tb^{3+} doped tetragonal ZrO_2 nanophosphors stabilized by Ba^{2+} ions, J. Lumin. 201 (2018) 303–313, https://doi.org/10.1016/j.jlumin.2018.05.003.

[92] J. Kohout, Modified Arrhenius equation in materials science, chemistry and biology, Molecules 26 (2021) 7162, https://doi.org/10.3390/molecules26237162.